UPPSALA
UNIVERSITET

Digital Comprehensive Summaries of Uppsala Dissertations from the Faculty of Science and Technology 1882

Interface Studies for Gold-based Electrochemical DNA Sensors

XINGXING XU

ACTA
UNIVERSITATIS
UPSALIENSIS
UPPSALA
2020

ISSN 1651-6214
ISBN 978-91-513-0824-1
urn:nbn:se:uu:diva-397807

Dissertation presented at Uppsala University to be publicly examined in Polhemsalen, Ångströmlaboratoriet, Lägerhyddsvägen 1, Uppsala, Monday, 20 January 2020 at 09:15 for the degree of Doctor of Philosophy. The examination will be conducted in English. Faculty examiner: Professor Boukherroub Rabah (French National Centre for Scientific Research, France).

Abstract
Xu, X. 2019. Interface Studies for Gold-based Electrochemical DNA Sensors. *Digital Comprehensive Summaries of Uppsala Dissertations from the Faculty of Science and Technology* 1882. 83 pp. Uppsala: Acta Universitatis Upsaliensis. ISBN 978-91-513-0824-1.

Gold based label-free electrochemical DNA sensors have been widely studied for biomarker diagnostics. The sensitivity and reproducibility of these sensors are determined by the sensing interface: the DNA modified gold surfaces. This thesis systematically studies the preparation processes of the DNA sensor interfaces as well as their effects on the sensor performance. First, three pretreatment methods to clean the gold electrode surface and their influence on the subsequent binding of thiolated molecules were carefully investigated. As we found that the surface pretreatment method involving cyclic voltammetry (CV) in H_2SO_4 may induce structural changes to the gold surface, thus greatly impacting the thiolated molecule binding, the factors influencing this pretreatment method were studied. Practical guidelines were summarized for preparing a clean and reproducible gold surface prior to functionalization. Afterwards, the effects of the surface coverage density of probe DNA and the salt concentration on the probe-target DNA hybridization on a gold sensing surface were systematically investigated using surface plasmon resonance (SPR) analysis. Based on the SPR results, the maximum potentiometric signal that could be generated by the DNA hybridization on the surface, and the detection limits, were estimated for different experimental conditions. These estimations were further compared with experimental results obtained using silicon nanowire field effect transistors (SiNW FET) with DNA modified gold on the gate oxide. Practical limitations for the potentiometric DNA sensor were analysed and discussed. Finally, the stability and reproducibility issues on the electrochemical impedance spectroscopy (EIS) analyses of DNA hybridization were also studied on the aptamer/mercaptohexanol (MCH)-modified gold surface. The root cause for the drift problems in this type of sensor and the temperature effects on the aptamer/MCH modified surface were identified. This thesis could serve as a practical reference for the preparation and understanding of the sensing interface of gold-based electrochemical DNA sensors.

Xingxing Xu, Department of Engineering Sciences, Solid State Electronics, Box 534, Uppsala University, SE-75121 Uppsala, Sweden.

ISSN 1651-6214
ISBN 978-91-513-0824-1
urn:nbn:se:uu:diva-397807 (http://urn.kb.se/resolve?urn=urn:nbn:se:uu:diva-397807)

I have met many magic phenomena during my PhD study. But I hope this thesis is scientific enough for those who meet the same magic as me.

To my beloved family
To my dear supervisors
To all the people who helped me

List of Papers

This thesis is based on the following papers, which are referred to in the text by their Roman numerals.

I Makaraviciute, A., **Xu, X.**, Nyholm, L., & Zhang, Z. (2017) Systematic approach to the development of microfabricated biosensors: Relationship between gold surface pretreatment and thiolated molecule binding. *ACS Applied Materials & Interfaces*, 9(31), 26610-26621

II **Xu, X**., Makaraviciute, A., Pettersson, J., Zhang, S.-L., Nyholm, L., & Zhang, Z. (2019) Revisiting the factors influencing gold electrodes prepared using cyclic voltammetry. *Sensors and Actuators B: Chemical*, 283, 146-153.

III **Xu, X.**, Makaraviciute, A., Abdurakhmanov, E., Wermeling, F., Li, S., Danielson, H, Nyholm, L., Zhang, Z. Estimating detection limits of potentiometric DNA sensors using surface plasmon resonance analyses. (*Minor revision submitted to ACS Sensors)*

IV **Xu, X.**, Makaraviciute, A., Kumar, S., Wen, C., Sjödin, M., Abdurakhmanov, E., Danielson, H, Nyholm, L., Zhang, Z.(2019) Structural Changes of Mercaptohexanol Self-assembled Monolayers on Gold and their Influence on Impedimetric Aptamer Sensors. *Analytical Chemistry,* 91(22), 14697-14704

Contributions to the papers

I. Designed and fabricated the gold electrodes, performed the electrochemical experiments and the results together with co-authors, performed XPS and AFM characterization and analyzed the results, and wrote part of the paper.

II. Designed the experiments together with co-authors, and performed all the experiments except ICP-MS, analyzed the data with the help of co-authors, and wrote the paper with input from all co-authors.

III. Designed the experiments together with co-authors, and performed the SPR and CC experiments with co-authors, analyzed the data, and wrote the paper with input from all co-authors.

IV. Designed the experiments with co-authors, and performed all the experiments, analyzed the data with the help of co-authors and wrote the paper with input from all co-authors.

Publications not included in the thesis

I. Zhang, D., Must, I., Netzer, N. L., **Xu, X.**, Solomon, P., Zhang, S. L., Zhang, Z., (2016). Direct assessment of solid–liquid interface noise in ion sensing using a differential method. *Applied Physics Letters*, 108(15), 151603

II. Pan, R., **Xu, X.**, Sun, R., Wang, Z., Lindh, J., Edström, K., Strømme, M., Nyholm, L., (2018). Nanocellulose modified polyethylene separators for lithium metal batteries. *Small*, 14(21), 1704371.

III. Tseng, C., Wen C., Huang, D., Lai C., Si Chen, Hu, Q., Chen X., **Xu, X.**, Zhang, S., Tao, Y., and Zhang, Z., (2019). Synergy of ionic and dipolar effects by molecular design for pH sensing beyond the Nernstian limit, Advanced Science, DOI: 10.1002/advs.201901001

IV. Palomar, Q., **Xu X.**, Cosnier, S., Gondran, C., Holzinger, M., Zhang, Z., Selective sensing of recombinant viral dengue virus 2 NS1 based on Au nanoparticles decorated multiwalled carbon nanotubes composites, submitted to *Sensors and Actuators B: Chemical*

Contents

1. Introduction and theoretical background 13
1.1. Emergence of electrochemical biosensors 13
1.2. Gold based electrochemical DNA sensors 14
1.3. Gold surface functionalization via SAM 14
1.3.1 SAM on gold 14
1.3.2. Defects in SAM 16
1.3.3. Probe DNA on gold and DNA hybridization regime 17
1.4. Label-free and electrochemical methods for detection of DNA and their limitations 18
1.4.1. Potentiometric DNA detection with ISFET 18
1.4.2. Limitations in potentiometric DNA detection with ISFET 19
1.4.3. EIS analysis of DNA hybridization 20
1.4.4. Limitations in EIS analysis 21
1.5. Scope of this thesis 22

2. Step-by-step fabrication and characterization methods for gold sensing electrodes 23
2.1. Gold electrode fabrication 23
2.2. Gold electrode pretreatment methods 24
2.3 Gold surface functionalization 25
2.3.1 Gold surface functionalization with DNA 25
2.3.2 Gold surface functionalization with DNA aptamer 25
2.4. Characterization methods 26
2.4.1 General introduction of electrochemical methods and measurement setup 26
2.4.2. CV of gold in H_2SO_4 27
2.4.3. Reductive desorption of MCH using CV 28
2.4.4. Chronocoulometry 29
2.4.5. EIS 30
2.4.6 Potentiometric measurements with ISFET 31
2.4.6. Surface Plasmon Resonance (SPR) 32
2.4.7. X-ray photoelectron spectroscopy (XPS) 32

3. Gold electrode pretreatment 33
3.1. Relationship between gold surface pretreatment and thiolated molecules binding 33

3.1.1. Characterizations of bare gold electrodes before and after three pretreatment methods....33
3.1.2. Characterizations of MCH-modified gold electrodes after different pretreatments....36
3.2. Factors influencing gold electrodes pretreated using CV in H_2SO_4....40
3.2.1. Experimental setups....40
3.2.2. Influence of Cl^- leakage from RE....41
3.2.3. Influence of platinum CE....43
3.2.4 Influence of Cl^- on platinum deposition....44
3.2.5. Origin of peaks in the EDL region....44
3.3. Practical guidelines for pretreating gold surfaces prior to functionalization....48

4. Sensor characterization....49
4.1. DNA hybridization on the gold surface....49
4.1.1. Tailoring the Γ_{Probe}....49
4.1.2. Relationship between the Γ_{Probe} and the target-probe DNA hybridization....50
4.1.3. Relationship of ionic strength and the target-probe DNA....51
4.2. Potentiometric detection of DNA....53
4.2.1. Estimation of the potentiometric signal for DNA detection....54
4.2.2 Potentiometric detection of DNA with gold coated-SiNW-FET....59
4.2.3. The limitations in the potentiometric DNA detection....61
4.3. EIS analysis of DNA hybridization on DNA aptamer/MCH modified gold....62
4.3.1. Irreproducible EIS results for aptamer/MCH modified gold electrodes after hybridization with P1....63
4.3.2. Drift in R_{CT} and C_{DL} for aptamer/MCH modified gold electrodes....65
4.3.3 Faradaic EIS analyses on aptamer/MCH modified gold after hybridization and after stabilization....66
4.3.4. Reasons for R_{CT} and C_{DL} drift for aptamer/MCH modified electrodes....67
4.3.5. Importance of stabilization process on hybridization signal....70

5. Summary....72

Sammanfattning på svenska....74

Acknowledgement....76

References....78

Abbreviations

$\Delta\varphi$	Change of surface potential
ε_0	Permittivity of free space
εr	Dielectric constant
λ_D	Debye length
μ	Electron mobility
ν	Scan rate
A	Electrode area
A_{geo}	Geometry area
C_{DL}	Double layer capacitance
CC	Chronocoulometry
CE	Counter electrode
CV	Cyclic voltammetry
C_{OX}	Oxide capacitance
C_0^*	Bulk concentration
D_0	Diffusion coefficient
dsDNA	Double strand DNA
e	Elementarty charge
E	Potential
EDL	Electric double layer
EIS	Electrochemical impedance spectroscopy
ESA	Effective surface area
E_{OC}	Open circuit potential
F	Faraday constant
f	Frequency
ISFET	Ion-selective field effect transitor
HER	Hydrogen evolution reaction
HOR	Hydrogen oxidation reaction
I	Ionic strength
I_{SD}	Source-drain current
ICP-MS	Inductively coupled plasma mass spetrometry
j	Current density
k_B	Boltzman constant
L	Length
MCH	Mercaptohexanol
n	Number of electrons per molecule
N_A	Avogadro number

$N_{nucleotide}$	Number of nucleotide within λ_D
Ox/Re	Gold oxidation and oxide reduction
P	Persistence length
P1	A short-length probe DNA complementary with aptamer
Q_{AuO}	Charge involving in reduction of gold oxide
Q_{DL}	Capacitive charge
Q_h	Net surface charge induced by hybridized target DNA
Q_{RE}	Charge involving in reductive desorption of MCH
R	Roughness factor
R_{CT}	Charge transfer resistance
$R_{CT, apt}$	R_{CT} at aptamer sites
$R_{CT, MCH}$	R_{CT} at MCH sites
RE	Reference electrode
RU	Response unit
R_S	Solution resistance
SAM	Self-assembled monolayer
SiNW	Silicon nanowire
ssDNA	Single-strand DNA
SPR	Surface plasmon resonance
STD	Standard deviation
STN	Signal-to-noise ratio
T	Absolute temperature in Kelvins
T_m	Melting temperature
TCEP	Tris(2-carboxyethyl)phosphine
Γ_0	Coverage density of adsorbed redox cations
Γ_{MCH}	Surface coverage density of MCH
Γ_{Probe}	Surface coverage density of probe DNA
Γ_{Target}	Surface coverage density of target DNA
V_G	Gate potential
V_T	Threshold voltage
ΔV_T	Threshold voltage shift
W	Width
WE	Working electrode
XPS	X-ray photoelectron spectroscopy
Z	Complex impedance
Z_{Im}	Imaginary part of Z
Z_{Re}	Real part of Z
Z_W	Warburg impedance

1. Introduction and theoretical background

With healthcare shifting towards early diagnostics and personal health management, increasing attention has been focused on direct biomarker detections and their applications in diagnostics, especially in point-of-care devices [1–3]. The main aim in biomarker-based diagnostics is to quickly collect information from as many biomarkers as possible and to analyze them for a global overview of the patient's health condition. This task requires fast, miniaturizable and easy-to-use devices, preferable with the capability of multiplex detection [4]. One important area of the research currently being carried out for this purpose is biosensors [5–7].

1.1. Emergence of electrochemical biosensors

A biosensor is a relatively simple analytical system consisting of a bioreceptor coupled to a signal transducer. Upon specific interaction with the analyte, the bioreceptor undergoes physical and chemical changes. These changes are registered by the transducer and converted to an output signal. Ideally, the output signal should be a function of the analyte concentration.

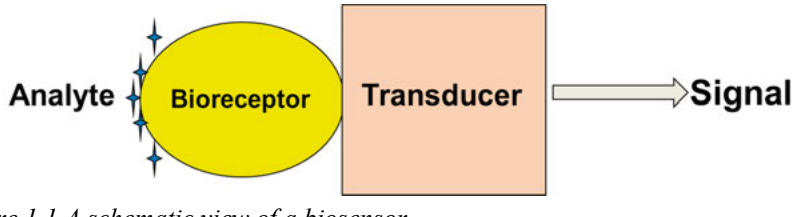

Figure 1.1 A schematic view of a biosensor

In the recent decades, electrochemical biosensors have been one of the major interesting research subjects due to high sensitivity, rapid response, label-free quantification, and low cost [5,8]. An electrochemical biosensor is a biosensor with an electrochemical transducer [5]. Various electrochemical methods, such as voltammetry [9], chronocoulometry (CC) [1], electrochemical impedance spectroscopy (EIS) [10] and potentiometry [11] have been employed in the development of electrochemical biosensors.

1.2. Gold based electrochemical DNA sensors

Electrochemical DNA sensors commonly consist of a single-strand DNA (ssDNA) with known sequence on the transducer surface, which is used as the bioreceptor to detect its complementary target strand [10,12]. The high affinity between two complementary DNA strands makes the recognition event (DNA hybridization) rapid and selective. Moreover, the intrinsic negative charge on the DNA phosphate backbones enables multiple choices of electrochemical detection methods [13]. For example, the negatively charged DNA can repel the negatively charged redox molecules (i.e., ferri- and ferrocyanide) [10]. The hybridization of the probe-target DNA can then change the charge transfer behavior between the redox molecules and the electrode. The quantitative information of the target DNA could be reflected as either the change of redox current registered by voltammetric methods, or the change of charge transfer resistance (R_{CT}) registered by EIS [14]. Moreover, the negatively charged DNA could also directly cause changes in either capacitive behavior or surface potential and both changes could be registered using an ion-selective field effect transistor (ISFET) [11,15].

Thiol-modified DNA can be immobilized on a gold surface easily via a self-assembly process based on thiol-gold chemistry [9]. Due to the ease of formation of a self-assembled monolayer (SAM) and the chemically inert properties of gold, gold-based electrochemical DNA sensors have been widely adopted. Usually a linker, typically mercaptohexanol (MCH), is linked to the ssDNA therefore allowing straightforward immobilization of ssDNA.

1.3. Gold surface functionalization via SAM

The functionalization of a gold surface with DNA (e.g., ssDNA or DNA aptamer) is via a self-assembly process. A smart interface design should also consider many issues, such as controlling the surface coverage density of the probe DNA (Γ_{Probe}) and the conformation of the probe DNA, minimizing avoiding non-specific interactions. A better understanding about the SAM modified gold surface can benefit the interface design.

1.3.1 SAM on gold

The preparation of a SAM is easy to perform and can be done both in gas phase and in liquid environments (from solutions of different solvents) [16]. Figure 1.2 depicts a simplified schematic view of the self-assembly process. The reaction between the thiol and gold is shown as Equation 1.1

$$RSH + Au \rightarrow RS - Au + \frac{1}{2} H_2 \qquad \text{Equation 1.1}$$

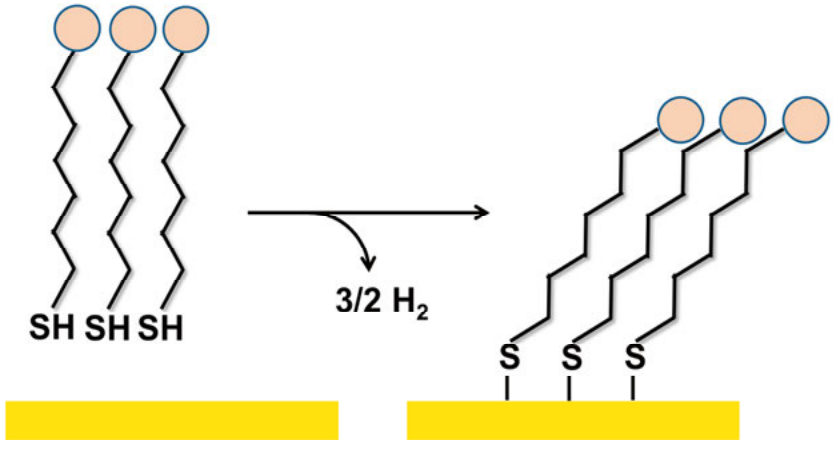

Figure 1.2. A schematic view of the formation of an alkanethiol SAM on Au.

The SAM on gold usually have relatively high stability due to Au-S bonds with the substrate and van der Waals interactions between molecules [16,17]. Figure 1.3 depicts a typical alkylthiol on gold, adopting a standing conformation. The thiol molecule consists of three parts. The first part is the sulfur head group, which forms a strong, covalent bond with the gold substrate. The energy for the Au-S bond is approximately 40 kcal/mol. The second part is a hydrocarbon chain (of variable length), which stabilizes and crystallizes the SAM through van der Waals interactions. Usually, the energy for van der Waals interaction between hydrocarbon chains is 1–2 kcal /mol per methylene. A relatively longer hydrocarbon chain could result in a better organized SAM. Thirdly, there is a terminal group, which determines the functionalities of the SAM. By tailoring the terminal group of the thiol, the physical and chemical properties of the SAM can be changed [18]. For example, –COOH, $–NH_2$ or –OH groups yield hydrophilic surfaces, which can decrease the non-specific adsorption of biomolecules.

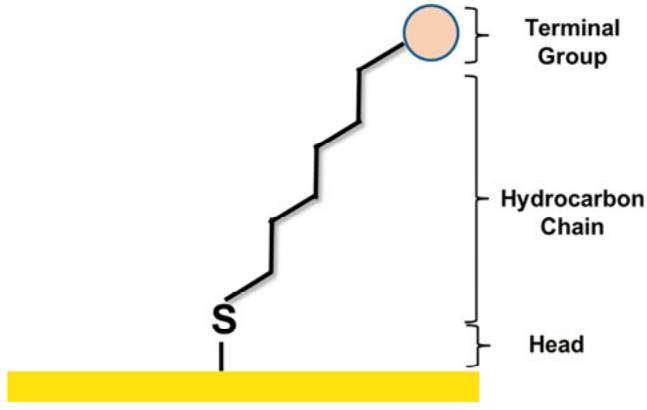

Figure 1.3. Scheme of an alkylthiol adsorbed on Au (yellow) in a standing up configuration.

1.3.2. Defects in SAM

Theoretically, SAMs form highly ordered interfaces with few defects, due to the thermodynamically-driven self-assembly process [19,20]. However, in practice many defects can occur in SAMs [17], which could be due to many factors as shown in Figure 1.4.

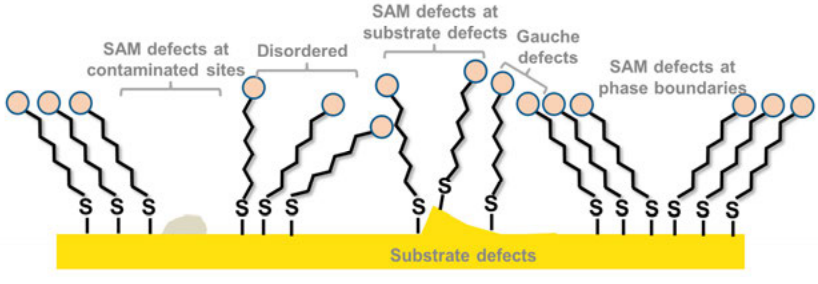

Figure 1.4. Schematic illustration of possible defects in SAMs formed on gold surface

The quality of SAMs is highly dependent on the cleanliness and the structure of the gold substrates. Contaminations on the gold surface could block binding sites, thus causing defects. Moreover, defects are very often found on gold grain boundaries [21]. Besides, some defects may be due to some intrinsic factors [17]. As is known, the SAM forms within a few minutes but the reorganization takes time [16].Pinholes, and gauche defects usually could be found on the well-ordered SAM [19]. Large defects, such as liquid-like domains, or regions with other phase domains can also occur [22]. On the other hand, the introduction of terminal groups (–SH, –COOH, –OH, $–NH_2$) different from the $–CH_3$ group usually results in a decrease in SAM ordering

because they add another strong interaction between adsorbate molecules [16].

1.3.3. Probe DNA on gold and DNA hybridization regime

A ssDNA is a kind of large, flexible and negatively-charged molecule. When the probe DNA is immobilized on the surface, the structure of probe DNA and the DNA hybridization behavior on the surface are highly dependent on the Γ_{Probe} and the salt concentration in the buffer. [23,24]

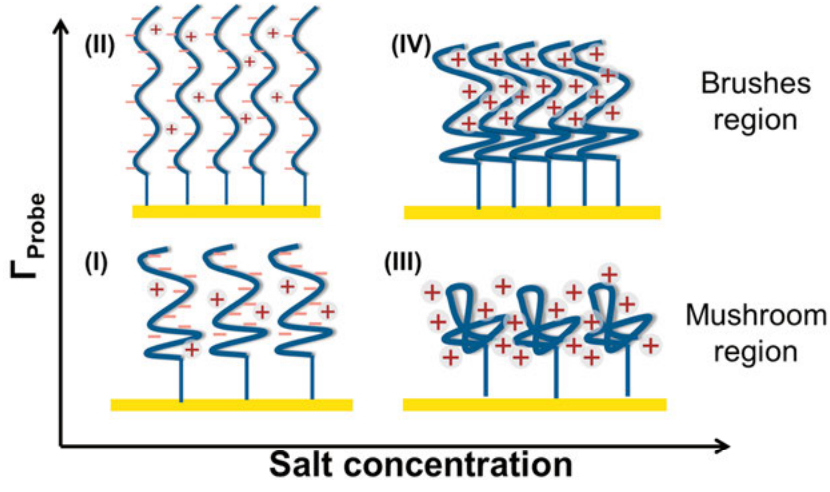

Figure 1.5. A schematic view of the influence of salt concentration and Γprobe on the DNA conformation on the gold surface.

The starting model for a ssDNA modified surface is a Langmuir isotherm [25]. At low Γ_{Probe}, it is assumed that DNA molecules do not interact with each other (the mushroom region) [23]. The hybridization efficiency is usually higher in this region. Increasing the Γ_{Probe} could give rise to the formation of polyelectrolyte brushes, leading to deviations with the Langmuir isotherm [12]. In this region, the interactions between the neighboring DNA molecules are enhanced, which could decrease the DNA hybridization efficiency and rate. Therefore, it is essential to control the Γ_{Probe}.

The persistence length (P), defined as "the length over which the tangent vectors at different locations on the chain are correlated", is a parameter describing the flexibility of the DNA.[26] Usually, P is 1-2 nm for a ssDNA [26]. The ssDNA as a probe in the DNA sensor is usually between 16 and 30 nucleotides, corresponding to a contour length (the maximum physical length) of 10-18 nm (assuming 0.60 Å/base). This suggests the ssDNA is very flexible. The flexibility of ssDNA can be influenced by the salt concentration of the buffer. In a low salt concentration buffer, the repulsion between the negatively charged phosphate backbones is high, resulting in an

increased P, thus decreasing the flexibility of the ssDNA. Increasing the salt concentration could shield more negative charge thus decreasing P. Furthermore, for the same reason, DNA hybridization is also affected by the salt concentration. Lowering the salt concentration could decrease the hybridization efficiency and rate. Therefore, a high salt concentration is beneficial for high hybridization efficiency.

Moreover, P is around 50 nm for a double strand DNA (dsDNA). Therefore, dsDNA is more rigid than ssDNA. The variations in flexibility of the ssDNA and the dsDNA suggest there will be a conformation change of the DNA upon hybridization. Usually, the hybridization could enable the twisted ssDNA to form a linear dsDNA. This conformational change should also be considered during the sensor development.

1.4. Label-free and electrochemical methods for detection of DNA and their limitations

1.4.1. Potentiometric DNA detection with ISFET

Potentiometric detection with FET is a label-free approach for detection of DNA with direct electrical readout [27]. Due to the properties of rapid response, sensitivity, and compatibility with CMOS technology, it has attracted much attention in recent years [15,28–30]. Figure 1.6 depicts a schematic view of an ISFET DNA sensor with gold substrate. In this ISFET DNA sensor, the gate surface is modified with probe DNA, using Au-S bonds.

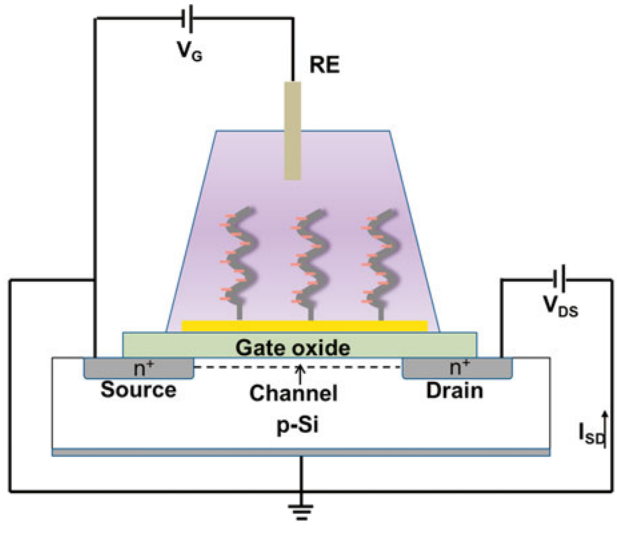

Figure 1.6. A schematic view of an ISFET DNA sensor. The gate oxide is coated with gold for DNA immobilization via gold-thiol chemistry.

In an ISFET DNA sensor, the source and drain current (I_{SD}) can be expressed by Equation 1.2 [31]:

$$I_{SD} = C_{OX}\mu\frac{W}{L}\left[\left(V_G - V_T\right)V_{DS} - \frac{1}{2}V_{DS}^2\right] \qquad \text{Equation 1.2}$$

Where C_{OX} is the oxide capacitance per unit area, W and L are the width and length of the channel, μ is the electron mobility in the channel. V_G is the applied gate potential. V_{DS} is the applied source-drain potential. Both V_G and V_{DS} can be kept constant during the measurement. V_T is the threshold voltage of the ISFET. The DNA hybridization at the sensor surface causes the accumulation of additional net negative charge on the gate surface. The additional negative charges could effectively change the V_T of the ISFET, thus changing the $I_{SD,}$ provided both V_G and V_{DS} are constant. It is also worth noting that due to the charge screening effect, only the additional charge within the Debye length [32] (λ_D, shown as Equation 1.3) could electrostatically change the V_T and be registered by the ISFET measurement.

$$\lambda_D = \sqrt{\frac{\varepsilon_r\varepsilon_0 k_B T}{2\times 10^3 N_A e^2 I}} \qquad \text{Equation 1.3}$$

In Equation 1.3, I is the ionic strength of the electrolyte in molar unit, ε_0 is the permittivity of free space, ε_r is the dielectric constant, k_B is the Boltzmann constant, T is the absolute temperature in Kelvins, N_A is the Avogadro number and e is the elementary charge.

1.4.2. Limitations in potentiometric DNA detection with ISFET

Numerous publications have reported the development of ISFET-based label-free detection of DNA molecules [15,33]. However, the results of potentiometric detections of DNA differ largely from report to report. One of the limitations in the potentiometric DNA sensing is the contradicting requirements for the charge registration and DNA hybridization. As Equation 1.3 shows, a lower ionic strength could yield a longer λ_D. Given a certain surface coverage density of target (Γ_{Target}) induced by DNA hybridization, a longer λ_D means that more negative charges on the hybridized DNA phosphate backbones could locate within λ_D, thus contributing to the potentiometric signal. However, as discussed in section 1.3.3, lower ionic strength at the same time enhances the repulsion between negatively charged DNA phos-

phate backbones, and thus reduces DNA hybridization efficiency. Moreover, the conformational change before and after DNA hybridization could cause charge redistribution.[12,23] As a ssDNA usually adopts a twisted structure and a dsDNA is more linear, it is difficult to know the absolute charge change within λ_D upon DNA hybridization, considering the charge redistribution effect. Furthermore, the sensing surface could also interact with other charges in the liquid sample; these interactions may buffer the signal generated by the DNA hybridizations if they are more overwhelming. Finally, potential drift is very often observed during potentiometric measurements. However, the reason for the drift is very complicated. It can be from the solid-state device or from the interface interactions. The noise level in the sensing system can also be the limiting factor for the low detection limits of DNA.

1.4.3. EIS analysis of DNA hybridization

EIS belongs to the most sensitive tools for label-free analysis of DNA hybridization [34]. Moreover, EIS is harmless to the DNA SAM modified surface compared to voltammetry or chronocoulometry since EIS measurements are usually performed at open circuit potential (E_{OC}) with a small excitation signal, which avoids the use of a ramping potential bias [14].

EIS detection of DNA is usually based on the repulsion between the negatively charged DNA with negatively charged ferri- and ferrocyanide redox molecules [12]. EIS measurements on DNA-modified gold surfaces usually yield a semicircle at high frequencies and a straight line with a slope corresponding to an angle of 45˚ (ideally) at low frequencies, when plotting the results as Nyquist plots (Figure 1.7). Information regarding the R_{CT} and double layer capacitance (C_{DL}) can then be extracted by fitting the data to the Randles equivalent circuit model [34,35]. R_{CT} could reflect the ability of the surface to block to ferri- and ferrocyanide molecules and the C_{DL} could reflect the DNA layer thickness and the gold electrode area. The DNA hybridization could thus modulate the concentration of the ferri- and ferrocyanide molecules near the gold electrode and cause R_{CT} changes.

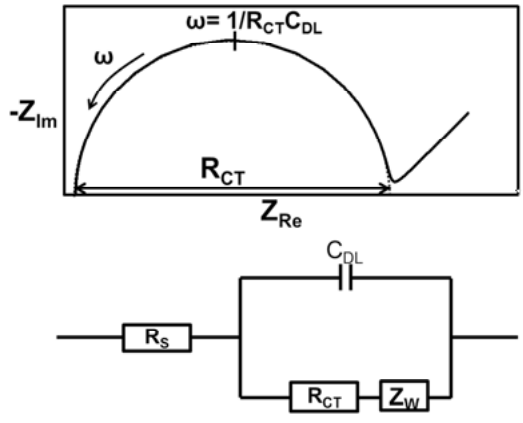

Figure 1.7. A typical Nyquist plots (up figure) with ferri- and ferro cyanide as a redox probe fitted with Randles equivalent circuit model (bottom figure). Z_{Im} depicts the imaginary part of the complex impedance (Z), Z_{Re} depicts the real part of Z, $\omega=2\pi f$ represents for the frequency (f), R_S is the solution resistance, R_{CT} is the charge transfer resistance, C_{DL} is the double layer capacitance, Z_W is the Warburg impedance.

R_{CT} changes induced by the hybridization of target DNA can be either positive or negative, which is dependent on not only the accumulation of additional negative charge on the surface but also the physical blocking of the access of the redox molecules to the electrode surface [12]. Upon DNA hybridization, more negative charge should be present on the surface, which could result in an increased repulsion of the negatively charged ferri- and ferrocyanide complexes. This should decrease the ferri- and ferrocyanide concentrations near the electrode surface which should result in an increase in R_{CT}. However, ssDNA is less rigid compared to dsDNA as illustrated in 1.3.3. After the hybridization, the twisted ssDNA can be stretched to a more linear state, yielding a reduced blocking of ferri- and ferrocyanide thus decreasing the R_{CT} [10]. As illustrated in Figure 1.5, the conformation of the ssDNA on the surface is dependent on both the Γ_{Probe} and the salt concentration. A smart sensor design should take these parameters into consideration.

1.4.4. Limitations in EIS analysis

Due to the sensitivity of EIS, a small change occurring on the sensor interface could lead to a significant R_{CT} change. This property is very beneficial to achieve high-sensitivity of the sensors. However, this also indicates that it can pick up R_{CT} change from other non-specific interactions or changes occurring on the interface, which can cause severe stability and reproducibility issues for the sensor. Therefore, to reliably measure the R_{CT} change caused by the DNA hybridization, one key requisite is that the biosensor interface is stable and reproducible during the acquisition of the spectrum [36]. Alt-

hough many articles have been published using EIS, few of them have addressed the inherent instability and non-reproducibility problems present within this type of system [37]. Commonly observed instability issue includes drift, which yields poorly reproducible EIS results [37–39]. EIS measurements on DNA/MCH modified gold have shown the drift when repeating the measurement multiple times [39]. Moreover, the drift was also observed on the protein modified surface. It has been reported that an increase in R_{CT} may not only be seen as a result of the target binding but also occurs i) when performing the measurements several times, ii) after subsequent voltammetric measurements, or iii) as a result of incubations in a buffer between the measurements [37]. Without proper understanding of the origin of the drift, the increase in R_{CT} can be misinterpreted as a positive signal [37]. If the R_{CT} drift is significant, it clearly becomes difficult to acquire reliable analytical results.

1.5. Scope of this thesis

This thesis aims at a comprehensive investigation of the factors influencing the performance of gold-based electrochemical DNA sensors during the surface preparation and the sensor characterizations. Since microfabricated gold electrodes are used in this thesis and the gold surfaces are contaminated after the microfabrication process, the gold surface needs to be pretreated prior to surface functionalization. ***Paper I*** compares three pretreatment methods, i.e., (i) CV in dilute H_2SO_4, (ii) gentle basic piranha incubation followed by linear sweep voltammetry in dilute KOH and (iii) oxygen plasma treatment followed by incubation in ethanol. These methods were compared in terms of cleaning efficiency, reproducibility and thiolated molecule binding. It has been found that structural changes can be induced to gold surfaces by "CV in dilute H_2SO_4" pretreatment and that these changes can influence the thiolated molecule binding. Therefore, ***Paper II*** studies the factors influencing gold surface prepared by this pretreatment method. ***Paper III*** demonstrates the combined effects of the Γ_{Probe} and salt concentrations on the DNA hybridization by using surface plasmon resonance (SPR) analysis. Finally, two types of electrochemical sensors are characterized. ***Paper IV*** investigated the stability issue of the aptamer/MCH modified gold surface on the EIS analysis of DNA aptamer hybridization.

2. Step-by-step fabrication and characterization methods for gold sensing electrodes

As the performance of the DNA sensor is highly dependent on the surface preparation and the detection method, the fabrication of DNA sensors was characterized step by step. This section will describe how the experiments and characterization were conducted.

2.1. Gold electrode fabrication

Microfabrication processes are used to produce devices with dimensions in the micrometer to millimeter range. Moreover, microfabrication processes can fabricate a batch of electrodes in parallel, which not only reduce the cost but also enable production of electrode arrays with similar surface properties. In this thesis, the gold electrodes were fabricated with standard microfabrication processes.

Specifically, gold electrode chips were fabricated on optically polished PYREX borosilicate glass (Präzisions Glas & Optik, Germany). A 100 nm thick thermally evaporated gold layer on 10 nm titanium was patterned by a standard UV photolithography and lift-off process. SU-8 2002 photoresist was used to define the 0.00785 cm^2 (diameter 1 mm) and the 0.0707 cm^2 (diameter 3 mm) electrodes. There were two identical electrodes with different sizes, distributed symmetrically on the same chip. (Figure 2.1)

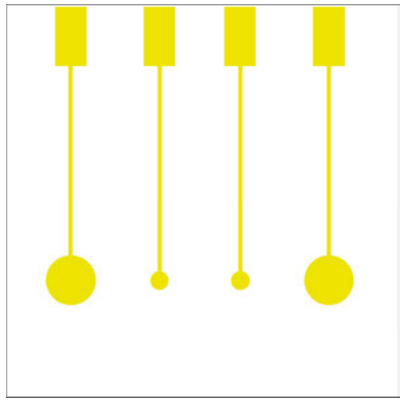

Figure 2.1. Schematic illustration of the size and location of the gold electrodes on the chips.

2.2. Gold electrode pretreatment methods

Three pretreatment methods adapted from literature [40] for cleaning gold surfaces prior to surface functionalization studied in ***Paper I*** were described below. The basic principle of these pretreatments is to oxidize the surface then reduce the possible gold oxide.

Dilute Basic Piranha and Linear Potential Sweep in Potassium Hydroxide. Au electrodes were incubated in 50 mM KOH and 25% H_2O_2 for 10 min and then rinsed with deionized water 5 times. Then electrode potential was linearly swept from −0.2 to −1.2 V at 50 mV/s scan rate (ν) in 50 mM KOH. Afterward the electrodes were rinsed with water and dried with N_2. This method is abbreviated to "KOH + H_2O_2 & LSV".

Cyclic Voltammetry (CV) in Dilute Sulfuric Acid. CV in 50 mM sulfuric acid solution is often used for cleaning and evaluating the state of gold electrodes.[41,42] Au electrodes served as working electrodes, and the potential was swept from −0.4 to 1.4 V for 15 cycles at a ν of 100 mV/s. After the CV, the electrodes were rinsed with water and dried with N_2. This method is abbreviated to "CV in H_2SO_4".

Oxygen Plasma Treatment and Ethanol Incubation. Au electrodes were cleaned in N_2 and O_2 plasma at 100 W for 5 min in a Tepla 300 plasma processor (PVA TePla, Germany). Since plasma treatment can damage the passivating SU-8 layer, the passivating layer thickness was measured before and after treatment. The plasma treatment parameters were optimized to not alter the passivating layer thickness. Afterward, the electrodes were incubated in ethanol for 30 minutes, rinsed with water, and dried with N_2. This method is abbreviated to "O_2 plasma & ethanol".

2.3 Gold surface functionalization

2.3.1 Gold surface functionalization with DNA

Au surface functionalization is usually achieved by thiol-gold chemistry. Basically, a MCH molecule is conjugated to the DNA thus enable direct immobilization of DNA on gold surface. By tailoring the probe DNA concentrations in the immobilization solutions (from 10 nM to 1 μM), different Γ_{Probe} can be achieved on the gold surface. Afterwards, the MCH molecule is applied to remove the non-specifically bonded DNA, to enable the sterically favorable DNA configuration, and to passivate the surface [43].

Thiol modified probe DNA is used in ***Paper III*** and ***IV*** with the following sequence:

5'-HO-$(CH_2)_6$-S-S-$(CH_2)_6$GCATTGGTCTACAAGTGAATCTCGA-3'

Specifically, the 50 μM probe DNA was reduced with 50 mM tris(2-carboxyethyl)phosphine (TCEP) for one hour at room temperature and diluted to different concentrations (10, 50, 100, 1000 nM in ***Paper III***). The probe DNA was heated at 95 ˚C for five minutes and cooled on ice for ten minutes prior to immobilization, in order to linearize the DNA. Then a freshly-pretreated gold electrode was incubated in solutions containing probe DNA for 16 hours at room temperature. Afterwards, the electrode was incubated in a tris buffer (10 mM Tris×HCl, pH 7.4) with 0.05% IGEPAL for five minutes with stirring to remove non-specific adsorption and then was incubated in the tris buffer for another five minutes to remove the surfactant. Afterwards, the electrodes were rinsed five times with tris buffer and were immediately incubated in 1 mM MCH in tris buffer for three hours to remove the non-specifically adsorbed probe DNA and to block the remaining gold surface area. After backfilling MCH, the electrode was washed as follows. First, the electrodes were washed with the tris buffer for 15 seconds and with the water for 15 seconds. Next, the electrodes were ultrasonicated in water for 30 seconds. Finally, the electrodes were rinsed with water for another 15 seconds.

2.3.2 Gold surface functionalization with DNA aptamer

Aptamers are synthetic oligonucleotides (RNA, ssDNA, etc.) or peptide molecules that can adopt secondary or tertiary structures after binding to certain targets with extremely high specificity [44]. Owing to the highly specific affinity of aptamers to target molecules, aptamers have been adopted as recognition elements in the development of ultrasensitive biosensors. In ***Paper IV***, a thiol modified DNA aptamer with 38 bases was used with the following sequence:

5'-HO-$(CH_2)_6$-S-
S$(CH_2)_6$GGGATGCCGTTTGGGCCCAAGTTCGGCATAGTGTGGTG-3'

Specifically, the 50 μM aptamer was reduced with 50 mM TCEP for one hour at room temperature and diluted with binding buffer (100 mM NaCl, 5 mM KCl, 2 mM $MgCl_2$, 1 mM $CaCl_2$, 20 mM Tris-HCl (pH 7.5)) yielding a final concentration of 5 nM. The aptamer was heated at 95 ˚C for five minutes and cooled on ice for ten minutes prior to immobilization. This heating step was used to linearize the aptamer and to decrease the self- and hetero-dimerization of the aptamers hence enabling a more uniform distribution. Then a clean gold electrode was incubated in 5 nM aptamer solution for 17 hours at room temperature. Afterwards, the electrode was incubated in the binding buffer for five minutes with stirring and then rinsed ten times with binding buffer. After washing, the aptamer-functionalized electrode was incubated in 1 mM MCH in the binding buffer for one hour to remove the non-specifically adsorbed aptamer and to block the remaining gold surface area. The electrode was washed with binding buffer ten times and directly employed in the electrochemical measurements.

2.4. Characterization methods

The main surface characterization methods used in this thesis are described here.

2.4.1 General introduction of electrochemical methods and measurement setup

Electrochemistry deals with the interrelation of electrical and chemical effects occurring at interfaces, namely the interface between a solid electrode and an electrolyte [35]. Electrochemical methods are very powerful and sensitive. Moreover, there are many electrochemical methods. Therefore, in the field of gold-based biosensors, electrochemical methods have been widely used in almost every step of the development of the sensors.

In ***Paper I-IV*** all the electrochemical experiments were performed using a VSP 300 electrochemical workstation (Bio-Logic, France). A conventional 3-electrode cell setup was used. The working electrode (WE) was the lab-fabricated gold electrode either with or without functionalization. The counter electrode (CE) was either a platinum wire (diameter 0.5 mm, ALS Co., Japan), a graphite rod, or a lab-fabricated gold electrode. All potentials were measured and are quoted against the Ag/AgCl/saturated KCl reference electrode (RE, ALS Co., Japan). The solutions used were degassed with N_2 for 30 min prior to each measurement. The temperature was room temperature (around 21 ˚C).

2.4.2. CV of gold in H_2SO_4

CV studies of gold in sulfuric acid solutions represent a powerful electrochemical approach for both gold surface pretreatments and analyses of the gold surface properties. During the CV measurement, a linearly-swept potential is applied to the gold electrode and then is reversed. The current flowing through the electrode/electrolyte interface in response to the potential is recorded. A redox reaction occurring on the electrode could give rise to a current increase, and a peak could be registered given a finite supply of the redox species.

In a typical cyclic voltammogram for gold in H_2SO_4 (**Figure 2.2**), three fingerprint regions have been conventionally defined[23]: the electric double layer (EDL) charging region where anion adsorption takes place, the gold oxide formation and subsequent reduction (Ox/Re) region where the different crystalline structures display characteristically different profiles, and the hydrogen evolution and oxidation reactions (HER/HOR) region where the catalytic performance of gold on HER can be assessed.

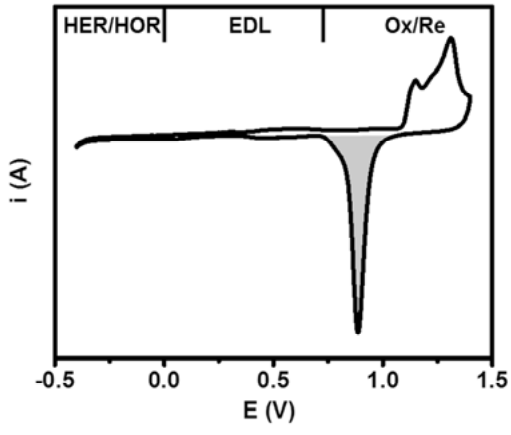

Figure 2.2. A typical cyclic voltamogram for gold in H_2SO_4 solution

The integration of the gold oxide reduction peak can determine the electrochemical surface area (ESA) of gold electrodes as described by Trasatti and Petrii.[42] This method has been used in ***Paper I-IV*** to pretreat the gold surface and characterize the ESA. Briefly, the CV measurement was performed in degassed 50 mM H_2SO_4 solution in the potential range from −0.4 to 1.4 V at a ν of 100 mV/s. Then the electrochemical surface area (ESA) was determined by the Q_{AuO} (the reduction charge). The latter was calculated by integrating the cathodic current profile area in the Ox/Re region. A theoretical value for polycrystalline gold of 400 μC/cm^2 was used under the assumption that oxygen was chemisorbed on Au in a one-to-one ratio.

The ESA can be expressed by roughness factor (R)

$$R = \frac{ESA}{A_{geo}} \qquad \text{Equation 2.1}$$

A_{geo} (0.00785 cm^2) is the geometric area of the electrode (diameter 1 mm) defined by SU-8 passivation.

2.4.3. Reductive desorption of MCH using CV

The SAM layer on the gold electrode can be reductively desorbed by applying a negative potential in a basic electrolyte. Figure 2.3 depicts a typical voltammogram for this reaction. The reductive desorption of one thiol consumes one electron (See Equation 2.2). Therefore, by calculating the amount of the electron transferred during the reduction, the surface coverage density of the SAM can be determined, given a certain electrode surface area.

$$S - Au + e^- \rightarrow Au + RS^- \qquad \text{Equation 2.2}$$

The surface coverage density can be used to evaluate not only the quality of this SAM but also the cleanliness and the structure of the gold surface.

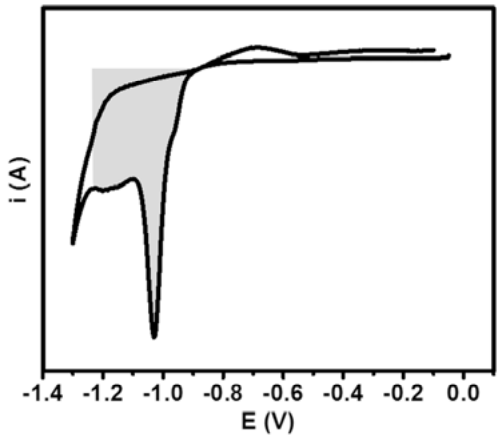

Figure 2.3. A typical cyclic voltamogram for reductive desorption of MCH on gold.

*In **Paper I***, pretreated gold electrodes were immersed in 1mM MCH aqueous solution for 1 h to form a SAM. To determine the Γ_{MCH}, reductive desorption was performed in degassed 100 mM KOH solution by means of CV. The potential was swept from 0 V to −1.3 V at a ν of 100 mV s^{-1}. The surface coverage density of MCH (Γ_{MCH}) was calculated as

$$\Gamma_{MCH} = Q_{RE} / \left(F \times A_{geo} \right) \qquad \text{Equation 2.3}$$

where Q_{RE} is the charge involved in MCH reductive desorption, F is the Faraday constant, and A_{geo} (0.00785 cm^2) is the geometric area of the electrode

(diameter 1 mm). To circumvent the contribution from the charging current, the baseline was set immediately before MCH reductive desorption. In the case of two peaks occurring, both peaks were integrated.

2.4.4. Chronocoulometry

With the negatively charged phosphate backbone, the DNA can electrostatically trap cations. When a DNA modified electrode is in a low ionic strength electrolyte with a multivalent redox cation, the redox cation could be electrostatically adsorbed on the DNA modified electrode. Usually, one phosphate could adsorb on redox cations. Therefore the Γ_{Probe} at the electrode surface can be calculated from the number of adsorbed redox cations [45].

The number of the trapped redox cations can be determined by CC. In this technique, a potential step is applied to the electrode and the resulting cumulative charge vs. time is observed (See Figure 2.4). The charge Q, as a function of time t in a CC experiment is given by the integrated Cottrell expression,

$$Q = \frac{2nFAD_0^{1/2}C_0^*}{\pi^{1/2}}t^{1/2} + Q_{DL} + nFA\Gamma_0 \qquad \text{Equation 2.4}$$

In the equation, n is the number of electrons per molecule for reduction, F is the Faraday constant (C/mol), A the electrode area (cm^2), D_0 is the diffusion coefficient (cm^2/s), C_0^* is the bulk concentration (mol/cm^2), Q_{DL} is the capacitive charge (C), and $nFA\Gamma_0$ is the charge from the reduction of Γ_0 (mol/cm^2) of adsorbed redox cations. The term T_0 represents the amount of redox marker confined near the electrode surface. The CC intercept at t = 0 is then the sum of the double layer charging and the charge from the reduction of adsorbed redox cations. The number of charges from the reduction of adsorbed redox cations can be determined from the difference of the CC intercepts measured with an identical potential step experiment in the presence and absence of the redox marker.

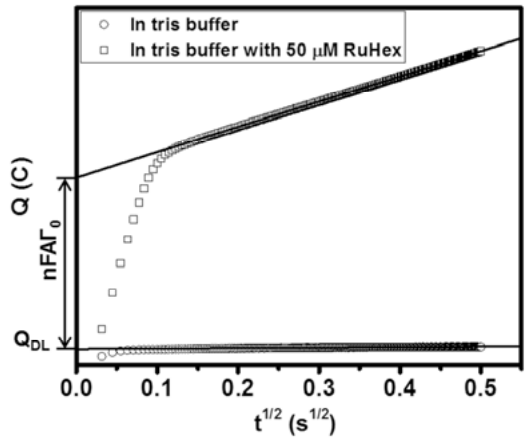

Figure 2.4. A typical CC result for DNA modified electrode in the presence and absence of RuHex. The open dots are the measured data and the solid lines are the fit of the linear region (diffusion part).

In ***Paper III*** and ***IV***, the CC measurements were conducted using tris buffer solutions with or without 50 μM RuHex. The CC was performed in the above solutions stepping from 0 to -350 mV with a pulse period of 250 ms. The time resolution was 1 ms.

2.4.5. EIS

As illustrated in section 1.4.3, EIS is a sensitive and versatile method in the development of biosensors. In this thesis, faradaic EIS measurements with the ferri- and ferrocyanide as the redox probe were performed to monitor the aptamer-P1 hybridization in ***Paper IV***.

The faradaic EIS measurements were conducted in binding buffer solutions containing 10 mM ferri- and ferrocyanide at room temperature (21 ˚C). The solutions used in all the EIS measurements had been degassed with buffer-saturated N_2 for over 30 minutes prior to the measurements. During the experiments, a flow of buffer-saturated N_2 was maintained above the solution to prevent oxygen from leaking in, as well as to limit evaporation of the solution. The solution mass was compared before and after an extended measurement and the results showed a difference of less than 1%. For all the EIS measurements, the results were based on 10 points in the range from 100 kHz to 0.1 Hz. To stay within the linear current-voltage region the ac potential amplitude was set to ±10 mV versus the open circuit potential. For all the measurements, the initial open circuit potential was 224 ± 1 mV and the open circuit potential changed less than 10 mV during the long time faradaic EIS measurements.

2.4.6 Potentiometric measurements with ISFET

The potentiometric detection of DNA was conducted using gold coated-silicon nanowire FET (SiNW-FET). The SiNW-FET was lab-fabricated. The SiNWs were coated with 40 nm-thick gold film (see Figure 2.5a and b), the latter are 500 nm wide, 1 µm long and 120 nm high. On each chip, half of the SiNWs were modified with probe DNA and the other half were modified with only MCH. The functionalization process was described in Section 2.3.1. The probe DNA concentration for the immobilization was 100 nM.

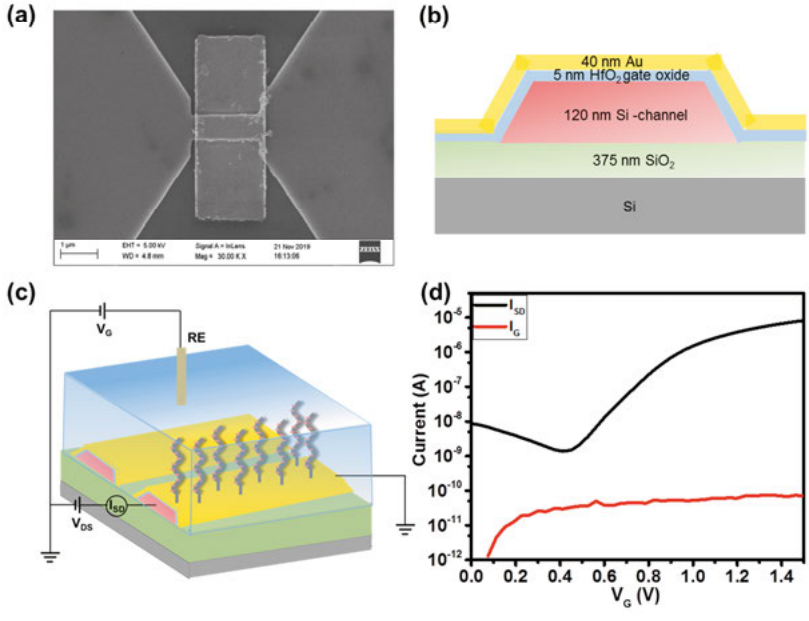

Figure 2.5. (a) SEM image of gold-coated SiNW FET. (b) Schematics of a cross section view of a gold coated-SiNW. (c) Schematics of the measurement setup. (d) The transfer curve of a gold coated-SiNW modified with probe DNA and MCH in tris buffer containing 10 mM NaCl.

Microfluidic system with Pump 11 Pico Plus Elite programmable syringe pumps (Havard Apparatus) was used for changing solutions. Microfluidic channel was fabricated with polydimethylsiloxane (PDMS, SYLGARD 184 Silicone Elastomer).

The potentiometric measurements were performed using HP4155 Semiconductor Parameter Analyzer. Upto 24 SiNWs can be measured simultaneously using a switching box (Keithley 3706). A schematic view of the measurement cell is shown in Figure 2.5c. A constant V_G was applied to RE, the V_{DS} was set to 1 V, and the I_{SD} current was monitored during the measurement. The I_{SD} was then converted to V_T shift (ΔV_T) based on the transfer curve (I_{DS} versus V_G) (see Figure 2.5d for an example).

2.4.6. Surface Plasmon Resonance (SPR)

SPR is a powerful optical technique to measure biomolecular interactions in real-time in a label-free environment. It is very sensitive to mass concentration change on the surface. Therefore, it can be used to quantify the adsorption-desorption or association-dissociation activities that take place on the surface.

In ***Paper III***, SPR is used to quantify the immobilized Γ_{Probe} and the hybridized target. The Γ_{Probe} was quantified by the SPR response decease prior to and after the DNA digestion by 1 Unit/μl benzonase nuclease. Usually, 1 SPR response unit (1RU) change is assumed to be equal to 1 pg/mm^2 mass concentration change. For the probe DNA, there are 7.84×10^{13} molecules in 1 μg. Therefore, 1 RU change corresponds to a Γ_{Probe} of 7.84×10^9 molecules/cm^2. The Γ_{Target} was quantified by the SPR response increase prior to and after probe-target hybridization. For the target DNA, 1 RU change corresponds to a Γ_{Target} of 7.88×10^9 molecules/cm^2.

2.4.7. X-ray photoelectron spectroscopy (XPS)

Based on the photoelectron effect[46], XPS was developed in the mid-1960's by Kai Siegbahn and his research group at Uppsala University, Sweden.[47] XPS is widely used to investigate the chemical composition of surfaces. It can measure the elemental composition, chemical state and electronic state of the elements within a material.

In ***Paper I*****,** XPS was used for analyzing the gold surface cleanness and the MCH surface. In ***Paper II***, XPS was used to detect the sulfate and chloride complexes formed on the gold surface. In both papers, XPS was performed on a Physical Electronics Quantum 2000 Scanning ESCA microprobe with monochromatized Al Kα radiation (hν = 1486.7 eV). The background pressure was 6.7×10^{-8} Pa (5×10^{-10} Torr). All spectra were referenced to Au 4f7/2 (84 eV). A spot of 100 μm and pass energy of 93.9 eV were used for survey spectra, and a pass energy of 23.5 eV was used for high-resolution spectra of C 1s and O 1s. The atomic concentrations were calculated using the sensitivity factor from Casa XPS software.

3. Gold electrode pretreatment

From section 1.3, we know that the gold surface functionalization based on thiol-gold chemistry is highly dependent on the gold surface cleanliness and the surface structure. The gold electrodes used in this thesis are microfabricated electrodes with SU-8 photoresist passivation, which can be severely contaminated during the fabrication process. To achieve efficient and reproducible surface functionalization, the gold surface should be cleaned with a reliable pretreatment method. In this chapter, different pretreatment methods were compared regarding the cleaning efficiency, the surface reproducibility and importantly, the influence on the thiolated molecule binding.

3.1. Relationship between gold surface pretreatment and thiolated molecules binding

3.1.1. Characterizations of bare gold electrodes before and after three pretreatment methods

Three pretreatment methods have been used to clean the gold surface, i.e., "O_2 plasma & ethanol", "H_2O_2 + KOH & LSV", and "CV in H_2SO_4". The detailed information about these three methods can be found in section 2.2 and in ***Paper I***. The surface cleanliness has been compared based on the elemental composition results from XPS and the ESA from the CV measurements.

Firstly, XPS survey spectra of microfabricated bare gold electrodes showed marked increases in carbon and oxygen signals indicating contamination. The elemental composition of the differently pretreated surfaces as well as the control sample (i.e., as-deposited gold surface) is provided in Figure 3.1. As the results show, the "O_2 plasma & ethanol" pretreatment was the most effective in terms of the gold element percentage. "H_2O_2 + KOH & LSV" pretreatment was the second most efficient method and "CV in H_2SO_4" was the least efficient with gold percentage increase.

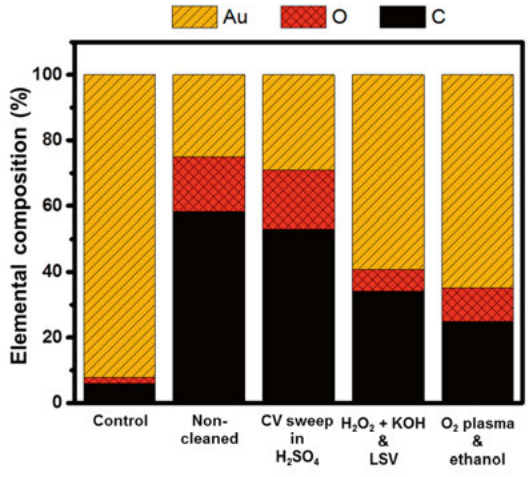

Figure 3.3. Elemental composition of gold electrode (diameter 1 mm) surfaces patterned with SU-8 photolithography before and after pretreatments of "KOH + H_2O_2 & LSV", "CV in H_2SO_4" and "O_2 plasma & ethanol".

In addition to XPS analysis, electrochemical evaluation of the ESA and its reproducibility was performed. ESA not only indicates the surface cleanliness but also reveals the relative quantity of sites available for thiol binding. For this reason, CV measurements were recorded in 50 mM H_2SO_4 in the potential range between -0.4 V and 1.4 V. The voltammograms of differently pretreated samples are shown in Figure 3.2. The integrated cathodic current profile areas are depicted in color.

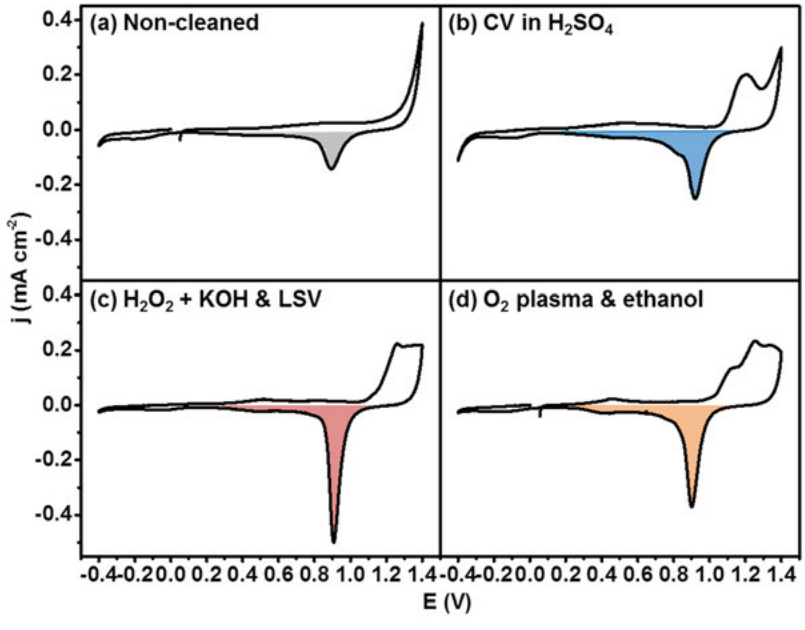

Figure 3.2. Cyclic voltammograms recorded in 50 mM H_2SO_4 for Au electrodes (diameter 1 mm) before and after using different pretreatment methods: (a) non-cleaned, (b) after "CV in H_2SO_4", (c) after "H_2O_2 + KOH & LSV" and (d) after "O_2 plasma & ethanol". The scan direction was positive and the scans were initiated at the potential of 0 V. The RE is Ag/AgCl/sat.KCl and the CE is Pt rod.

In the case of the non-cleaned SU-8 passivated electrode (Figure 3.2a), the gold oxidation peak was largely suppressed and the peak potential was shifted positively. This indicates that contamination strongly decreased the gold atom availability. Consequently, on the return scan the gold oxide reduction peak at ≈0.9 V also exhibited the lowest intensity out of all the investigated samples.

Large increases in the peak current accounting for the gold oxide formation were observed after all pretreatments. In the case of "H_2O_2 + KOH & LSV" (Figure 3.2c) and "O_2 plasma & ethanol" (Figure 3.2d) pretreatments, they yielded different oxidation current profiles. Distinct gold oxidation current profile shapes have been assigned to different surface crystallinities [48]. During the reverse sweep, increases in the gold oxide reduction peak current were observed as well.

Interestingly, electrodes exposed to "CV in H_2SO_4" pretreatment exhibited a notably different current profile shape than those pretreated by the other two methods. It had three distinct characteristics. First, the current in the gold oxide formation region was markedly elevated and constituted of two overlapping peaks at 1.15 V and 1.2 V. Second, the reduction peak was also split into two: a larger peak at 0.9 V and a smaller one at 0.8 V.

In order to evaluate reproducibility of the ESA, roughness factor R values were calculated and provided in Table 3.1. The detailed information of the calculation can be found in section 2.4.1 and ***Paper I***.

Table 3.1. R obtained from CV of Au in H_2SO_4 before and after using different pretreatments.

Pretreatment	R_{Mean}	R_{STD}
Non-cleaned	0.93	0.10
CV in H_2SO_4	1.50	0.14
H_2O_2 + KOH & LSV	1.34	0.11
O_2 plasma & ethanol	1.39	0.06

Based on the student's t-test, statistically significant differences in the R values were observed when comparing non-cleaned and differently pretreated electrodes. The increase in the R value was up to 1.5 times for "O_2 plasma & ethanol" pretreated surface. However, no significant differences were observed among the R values obtained after different pretreatments including "CV in H_2SO_4" pretreatment, which exhibited a distinct current profile shape. Furthermore, the reproducibility values of both non-cleaned surfaces and the pretreated surfaces were not statistically different according to the F-

tests. Thus, despite the observed differences in cleanliness and surface structure, all three surface pretreatments equally effectively increase R in comparison to that of the non-cleaned electrodes.

3.1.2. Characterizations of MCH-modified gold electrodes after different pretreatments

After the evaluation of bare gold electrodes, the effect of surface pretreatment on thiolated molecule binding was evaluated. For this reason, a MCH SAM was formed on differently pretreated electrodes.

The Γ_{MCH} was calculated by integrating the MCH reductive desorption peak at around -1 V. Moreover, the reductive desorption peak position, its area and shape reflect the adsorption energy, stability, coverage and morphology of the monolayer. Voltammograms of MCH reductive desorption are shown in Figure 3.3.

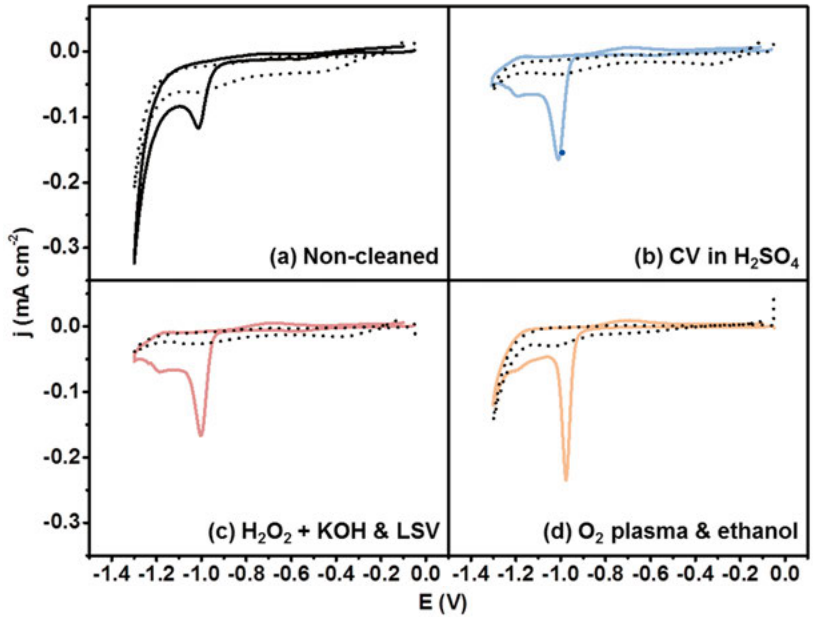

Figure 3.3. Reductive desorption of MCH (solid line) formed on Au electrodes (diameter 1 mm) patterned with SU-8 photolithography after using different surface pretreatments: (a) non-cleaned, (b) after "CV in H_2SO_4", (c) after "H_2O_2 + KOH & LSV" and (d) after "O_2 plasma & ethanol". Background current is depicted in a dotted line. Electrolyte was 100 mM KOH. The scan direction was negative, the ν *was 100 mV/s and the scans were initiated at the potential of 0 V. The RE is Ag/AgCl/sat.KCl and the CE is Pt rod.*

From Figure 3.3, it can be seen that after the electrodes were exposed to different pretreatment methods, the current profiles changed compared to the non-cleaned sample. First, increases in the peak current density of MCH

reductive desorption were observed. The extent of the increase varied slightly for each pretreatment method. The peaks were also narrower than the one registered on the non-cleaned electrode indicating more ordered MCH SAM structures on the pretreated electrodes. Additionally, small broad peaks traceable to oxidative MCH molecule re-adsorption were observed at -0.8 V on anodic scans after the investigated surface pretreatments. Finally, significant decreases in current at the negative potential limit were observed after all pretreatments.

However, it worth noting that after all the investigated pretreatments a second, broader peak at -1.2 V occurred. The highest intensity of this peak was observed after "CV in H_2SO_4" pretreatment. A search in the literature revealed that multiple peaks have been observed in some reductive desorption measurements but a consensus on their origin has not been reached.[49] The different explanations regarding the occurrence of the double peaks from the literature have been provided in ***Paper I***.

Since the majority of explanations from the literature do not convincingly explain the origin of the second peak, this uncertainty hampers the understanding of surface functionalization. It also leads to uncertainties in the determination of Γ_{MCH}. For instance, if the second peak arises from other phenomena than the reduction of the gold-thiol bond, it should not be included in the determination of Γ_{MCH}.

In order to investigate the origin of the second peak, partial reductive desorption of MCH was performed (See details in ***Paper I***). The sample was then analyzed by XPS (Figure 3.4)**.**

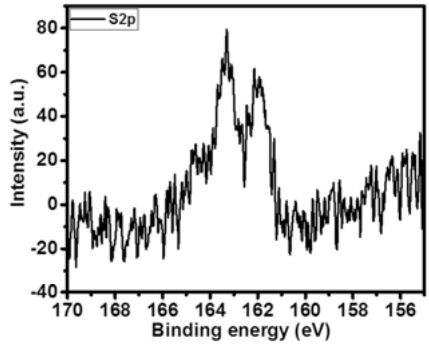

Figure 3.4. S2p spectrum of MCH on Au electrode surface after partial reductive desorption.

The S2p spectrum of the sample is shown in Figure 3.4. The $S_{2p3/2}$ peak at 162 eV is attributed to chemisorbed sulfur atoms. This result was in agreement with those reported in the literature.[50] Thus, it was confirmed that the second peak arises from reductive cleavage of the gold-thiol bond.

As mentioned before, the highest intensity of the second MCH reduction peak was observed after the "CV in H_2SO_4" pretreatment. Interestingly, this pretreatment also yielded the most distinct profile of the bare gold voltammogram indicating alterations in surface gold morphology. To explore the relationship of the two phenomena, a non-cleaned gold electrode was pretreated by "CV in H_2SO_4" for 50 cycles as opposed to the 15 cycles used earlier.

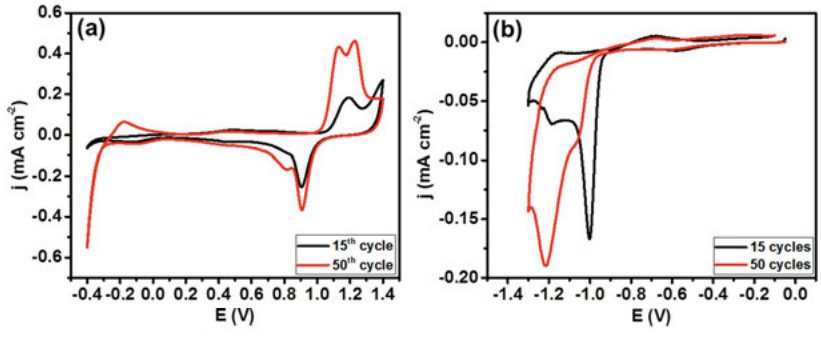

Figure 3.5. (a) Cyclic voltammograms recorded in 50 mM H_2SO_4 using bare Au electrodes and (b) reductive MCH desorption in 100 mM KOH after surface pretreatment by "CV in H_2SO_4" for 15 (black) and 50 (red) cycles. The ν was 100 mV/s.

The voltammograms of the 15th and 50th cycles for "CV in H_2SO_4|"were provided in Figure 3.5a. As it can be seen from the figure, after "CV in H_2SO_4" for 50 cycles the oxidation current was markedly increased and exhibited two well-defined peaks at 1.1 V and 1.2 V. The reduction peak at 0.9 V retained its intensity. However, the intensity of the reduction peak at 0.8 V increased significantly with increasing cycles.

These two pretreated electrodes were then incubated in MCH solutions and subjected to reductive desorption. The voltammograms are provided in Figure 3.5b. It showed a clear relation between the structural state of the surface and molecule binding. The intensity of the second peak at -1.2 V markedly increased with decreasing intensity of the peak at -1.1 V suggesting the formation of more stable gold-thiol complexes.

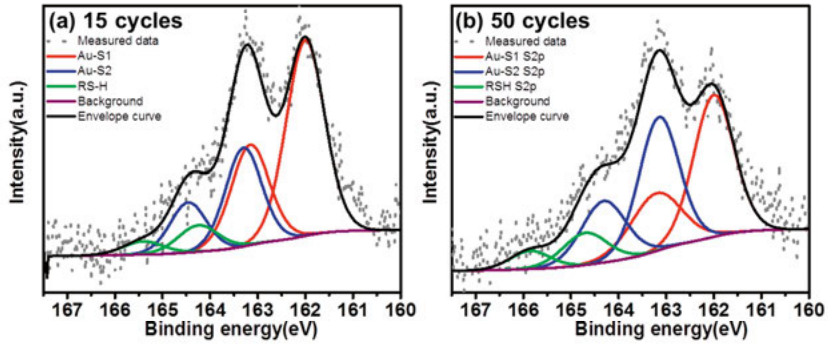

Figure 3.6. XPS S2p spectra of MCH adsorbed on Au electrodes pretreated by "CV in H_2SO_4" for (c) 15 and (d) 50 cycles.

The MCH formed on gold electrodes pretreated by "CV in H_2SO_4" for 15 and 50 cycles were further investigated with XPS. The S2p spectra of MCH formed on gold electrodes are provided in Figures 3.6. The S2 spectra of both samples were fitted to three doublets. A doublet with the $S2p_{3/2}$ peak at 162 eV (shown in red, Au-S1 has been attributed to the bound sulfur. No differences in the binding energy of this doublet between the two samples were observed. The $S2p_{3/2}$ peak of the second doublet (shown in blue, Au-S2 was located at 163.2 eV. Notably, with the CV cycle increasing from 15 to 50, this peak intensity increased pronouncedly. Such variations in gold-thiolate bonds could explain the correlation between the changed surface structures after the "CV in H_2SO_4" pretreatment, reductive desorption and photoemission spectra. The last doublet (shown in green, R-SH with the $S2p_{3/2}$ component at 164.3 eV for the 15 cycles swept electrode and at 164.7 eV for the 50 cycles swept electrode was attributed to the unbound sulfur species.

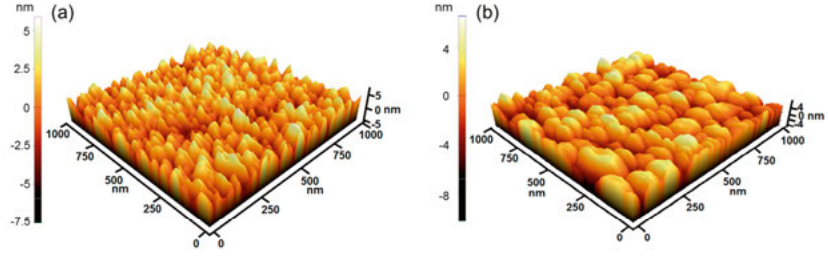

Figure 3.7. AFM results of Au electrodes after CV in 50 mM H_2SO_4 for (a) 15 cycles; (b) 50 cycles.

To demonstrate the reason for the different binding properties of thiolated molecules, AFM was performed on the gold surfaces after CV for 15 and 50 cycles (Figure 3.7). It can be seen that the grain sized increased with increasing CV cycles. The results suggest structural changes of the gold surface

after CV pretreatment may cause changes in the binding properties of the thiolated molecules.

Since it was determined that the second peak observed in the reductive desorption measurements arises from the gold-thiolate bonds, the areas of both peaks were integrated in order to calculate the Γ_{MCH} and their reproducibility before and after the investigated pretreatments. The calculated results of Γ_{MCH} before and after different pretreatments are provided in Table 3.2. Similarly to the case of bare gold electrodes, differences in Γ_{MCH} were statistically significant before and after different pretreatments based on t-test analysis. The average Γ_{MCH} was up to 2.75 times higher in the case of "O_2 plasma & ethanol" pretreatment. However, after "CV in H_2SO_4" and "H_2O_2 + KOH & LSV" pretreatments, the difference between these was insignificant. Interestingly, the highest reproducibility was obtained in the case of the non-cleaned electrode. However, when comparing different pretreatment methods, no significant differences in reproducibility among them have been observed.

Table 3.2. Γ_{MCH} on differently pretreated Au electrodes.

Pretreatment	Γ_{MCH} (mol cm^{-2})	
	Mean	STD
Non-cleaned	1.05×10^{-9}	6.92×10^{-11}
CV in H_2SO_4	2.09×10^{-9}	4.58×10^{-10}
H_2O_2 + KOH & LSV	2.19×10^{-9}	2.05×10^{-10}
O_2 plasma & ethanol	2.75×10^{-9}	3.95×10^{-10}

*The mean and STD were calculated from 4 different electrodes of each pretreatment method.

3.2. Factors influencing gold electrodes pretreated using CV in H_2SO_4

CV in H_2SO_4 electrolytes is a widely used method for surface preparation and characterization of gold electrodes in several research areas [41,51,52]. A standard CV pretreatment involves a gold WE in an oxygen-free H_2SO_4 solution, which is repeatedly swept in the potential range between -0.4 and 1.4 V with a Ag/AgCl/sat. KCl RE and a platinum CE [51,52]. However, we have found that structural changes can be induced to gold surfaces by the standard CV pretreatment and that these changes can influence the thiolated molecule binding [52]. Therefore, in this section, the factors influencing the gold electrodes prepared using "CV in H_2SO_4" pretreatment is investigated.

3.2.1. Experimental setups

From the literature, we found that some factors originating from the experimental setup (i.e., the Ag/AgCl/sat.KCl RE and the platinum rod CE) may

affect the shape of the voltammograms, thus may change the gold structure after the CV pretreatment. One of the factors could be Cl^- released into the electrolyte from the RE as this may lead to the formation of soluble gold-chloride complexes during the anodic scan and hence etching of the gold electrode [53,54]. Some of the dissolved gold is re-deposited on the WE on the return scan giving rise to a new cathodic peak at more negative potentials compared to the potential of the gold oxide reduction peak [55]. Another factor may come from the platinum CE. Some of the platinum may dissolve during the formation of platinum oxide [56]. If this occurs, the dissolved platinum could deposit on the gold WE thus changing the property of the gold surface [48,57]. Moreover, as the Cl^- can also react with platinum and form the soluble complexes, the dissolution of platinum can be accelerated if there is Cl^- leaking from the RE [35].
In order to obtain a more comprehensive understanding of the separate and interdependent effects of the aforementioned factors on gold surface prepared by "CV in H_2SO_4", a series of experiments using a conventional configuration including an Ag/AgCl/sat. KCl RE and a platinum CE (as schematically shown in Figure 3.8) were designed and tested.

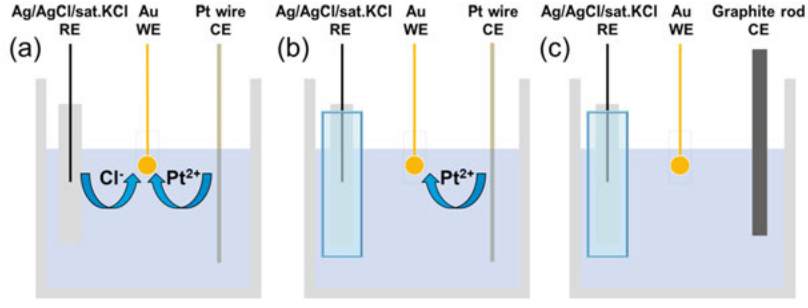

Figure 3.8. Schematic view of the experimental setups: (a) a conventional configuration with an Ag/AgCl/sat. KCl RE and a platinum wire CE; (b) an alternative setup with the RE placed in a bridge filled with the electrolyte; (c) an alternative setup with the RE placed in a bridge filled with the electrolyte and a graphite rod CE.

3.2.2. Influence of Cl^- leakage from RE

To investigate whether there was Cl^- leaking from the RE, CV experiments were conducted using the setups shown as Figure 3.8a and b, i.e., without and with a bridge. The bridge was serving as a double junction to eliminate the contamination of Cl^- leaking from the RE.

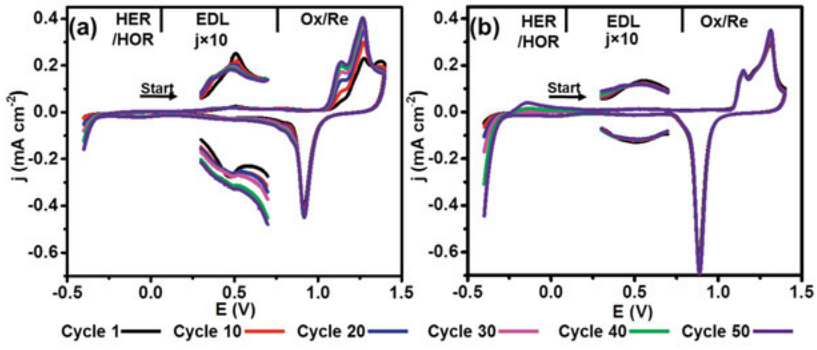

Figure 3.9. Cyclic voltammograms recorded in 50 mM H_2SO_4 *for gold electrodes with the experimental setup shown in (a) Figure 3.7a (b) Figure 3.7b. In the figures the current densities in the EDL region have been magnified by a factor 10, respectively.*

As shown in Figure 3.9a and b, the cyclic voltammograms shows clear differences between the setups with and without the bridge for RE. Firstly, the peaks in the Ox/Re region were not stable during the cycling when there was no RE bridge. In the gold oxidation region, the current at the positive limit of the potential range decreased whereas the size of the peaks at around 1.28 V and 1.14 V increased and the peak positions were also shifted slightly in the negative direction with increasing cycle number. On the reverse scan, the gold oxide reduction peak was registered at 0.92 V but an additional reduction peak shown like a shoulder also developed at around 0.80 V with increasing cycle number. In contrast, reproducible gold oxidation and reduction peaks were seen when the Cl^- leakage from RE was minimized with the bridge. Two gold oxidation peaks were registered at 1.14 V and 1.32 V while the subsequent reduction peak occurred at 0.89 V throughout the cycling. The disappearance of the shoulder during the reduction of gold oxide suggesting the shoulder at around 0.8 V was from the reduction of gold chloride complexes.

Secondly, a cathodic feature current, which could be attributed to the HER process, became apparent at potentials below -0.2 V during the cycling for both Figure 3.9a and b. With increasing cycle number, the HER current increased and the HER onset potential shifted in the positive direction. Interestingly the HER peak was more pronounced and the HOR current appeared when the Cl^- was minimized with the RE bridge (Figure 3.9b)

Finally, broad and small peaks were found at around 0.50 V for Figure 3.8a and around 0.6 V for Figure 3.9b in the EDL region. The peaks in both figures were slightly shifted in the negative direction with increasing cycle number.

The above observations confirm the leakage of Cl^- from the RE. However, there are still developing features in the HER/HOR region even with the

RE bridge. Interestingly, the HER/HOR currents profiles showed clear differences between the setups with and without the RE bridge. Moreover, the origin of the peaks in the EDL region is not clear. Therefore, more experiments were conducted to demonstrate these issues.

3.2.3. Influence of platinum CE

As the platinum CE was used during the measurements (see Figure 3.8a and b), the observed HER/HOR effect can most likely be ascribed to the result of catalytic properties of a deposition of dissolved platinum from CE on the gold WE [57]. It has been found that the dissolution of platinum takes place at potentials above 0.8 V in H_2SO_4 electrolytes [56,58]. In the present study, the potential of the platinum CE was found to reach values up to 0.96 V when Cl^- were present in the H_2SO_4 (i.e. without the RE bridge) whereas the corresponding potential was 1.35 V with the RE bridge. It is thus reasonable to assume that there was platinum dissolution from the CE both with and without the bridge and that the dissolved platinum could be deposited on the gold electrode during the cathodic CV scan.

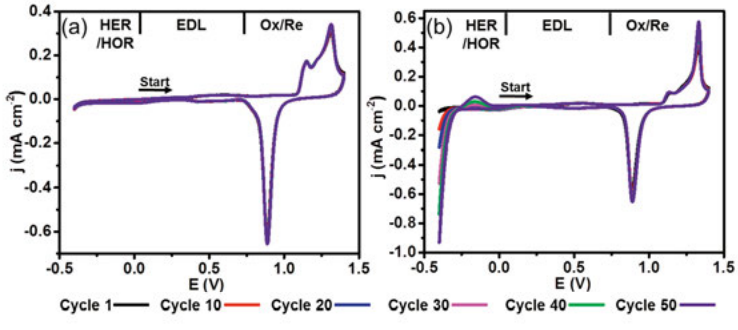

Figure 3.10. Cyclic voltammograms for gold electrodes recorded in 30 mL of 50 mM H_2SO_4 using the experimental setup shown in Figure 3.7c. (a) In 50 mM H_2SO_4 solution; (b) In 50 mM platinum-enriched H_2SO_4 solution. The Pt-enriched H_2SO_4 solution was prepared by CV with Pt rod as WE for 50 cycles in the range of 0.40 V to 1.35 V.

To further confirm that platinum deposition on the gold electrode was indeed the cause of the high HER catalytic performance, the Pt CE was replaced by a graphite rod (as seen in Figure 3.8c). As expected, the HER current then became negligible and did not increase with increasing cycle number (see Figure 3.10a). To further support this conclusion, CV experiments were conducted in a platinum-enriched H_2SO_4 solution (see the results in Figure 3.10b). The HER activity then increased with increasing cycle number as a result of the platinum deposition taking place upon each cycle (Figure 3.10b). It can consequently be concluded that the HER/HOR catalytic activity seen for the gold electrode was in fact due to platinum dissolving from the CE and depositing on the surface of the gold WE.

3.2.4 Influence of Cl^- on platinum deposition

When comparing the HER currents in Figure 3.9, it can be seen that the HER current actually was higher with than without the bridge, i.e. for a lower Cl^- concentration. This is unexpected since a lower Cl^- concentration would be expected to result in less dissolved Pt [59]. In order to cast more light on this problem, inductively coupled plasma mass spectrometry (ICP-MS) experiments were carried out to determine the concentrations of the dissolved gold and platinum species in the electrolyte after the experiments with and without the RE bridge. As seen in Table 3.3, the concentration of dissolved Pt species was indeed lower with than without the bridge (i.e. for a lower Cl^- concentration) as could be expected. The ratio between the platinum and gold concentrations was, however, much higher with the bridge. This demonstrates that the etch rate was significantly higher for platinum than for gold at the lower Cl^- concentration. This finding can then be used to explain the HER results as the surface concentration of Pt would be higher after the Cl^- leakage was minimized since less Au would be co-deposited together with Pt during the cathodic scan. When there was leaked Cl^-, the etching rate of the gold was increased and the co-deposition of Au and Pt would hence decrease surface concentration of Pt and therefore cause a less pronounced HER effect. The difference in the magnitude of HER current demonstrates that the electrochemical property of the Au electrode is determined by the ratio between the dissolved amounts of Au and Pt rather than the absolute amount of the dissolved Pt.

Table 3.3. Concentrations of dissolved platinum and gold species in the electrolytes after 50 CV cycles in 6 mL of 50 mM H_2SO_4.

Sample	Concentration (ng/ml)		Concentration ratio (C_{Pt}/C_{Au})
	C_{Au}	C_{Pt}	
Control	<0.1	<0.1	-
Without a bridge (Cl^- leakage)	183.9	21.7	0.13
With a bridge (smaller Cl^- leakage)	3.0	9.1	3.13

It should be noted that the deposited platinum on the gold WE should be less than one monolayer and could not be detected by XPS, but greatly impacted the electrochemical behavior of the gold electrode. It is therefore highly recommended to avoid use of a platinum CE.

3.2.5. Origin of peaks in the EDL region

As shown in Figure 3.9, small peaks were seen in the EDL region when cycling the gold electrodes in the H_2SO_4 electrolyte both with and without the

RE bridge. The peaks were, however, found at more negative potentials in the Cl^--containing electrolyte. Specifically, the peak on the anodic scan in Figure 3.9a (i.e. in the absence of the RE bridge) was found at around 0.515 V on the first cycle and at about 0.480 V on the 50th cycle. When using the RE bridge (see Figure 3.9b), a peak on the anodic scan nevertheless was seen at 0.555 V on the first anodic scan and this peak underwent slight broadening during the cycling. The change in the corresponding reduction peak was, on the other hand, less pronounced as a broad peak was seen throughout the experiment.

It was obvious that the peaks in the EDL region could be influenced by the Cl^- concentration. Moreover, as the other reasons for the peak in the EDL region, e.g., the surface reconstruction of the gold, the oxidization and reduction of metal or organic contaminations from the microfabrication process have been excluded (see **Paper *II*** for more information), the only remaining plausible reason for these peaks is due to the oxidation and reduction of the gold electrode, specifically, electron transfers accompanied by anion adsorption [60–62]. While such a partial or full charge transfer reaction has been proposed, the electrochemical reaction responsible for these peaks in the CVs has not yet been identified. This issue will therefore be investigated further below.

3.2.5.1. Influence of anion concentration on the peaks in the EDL region

In the literature it has been demonstrated that Cl^- and SO_4^{2-} can adsorb on the gold electrodes during the anodic scan and desorb in the cathodic scan respectively [63–65], and that adsorption of Cl^- is stronger than that of SO_4^{2-} [63,65,66]. Moreover, it should be mentioned that when metal-ion complexes (or ion-pairs) are formed, negative shifts in the peak potentials are generally observed with increased ligand concentrations [35]. To further investigate the relationship between the peaks in the EDL region and the anion concentration, CV measurements were conducted with gold electrodes in the potential range between 0 and 0.8 V using the experimental setup shown in Figure 3.7c for different concentrations of H_2SO_4 (see Figure 3.11a) as well as with different KCl concentrations in the H_2SO_4 solutions (see Figure 3.11b).

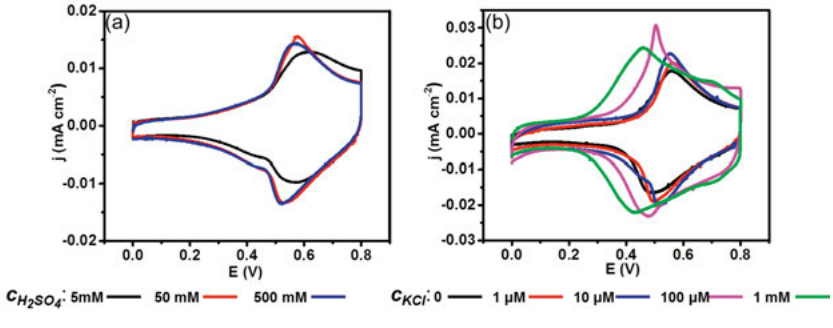

Figure 3.11. Cyclic voltammograms recorded for gold electrodes using the experimental setup shown in Figure 1c for different: (a) H_2SO_4 concentrations and (b) KCl concentrations in 50 mM H_2SO_4. Note that different current density axes are used in the voltammograms in a) and b).

As shown in Figure 3.11a, the oxidation peak potential gradually shifted from 0.678 V to 0.564 V with the H_2SO_4 concentration increasing from 5 mM to 500 mM. A calculation of the peak charge, however, showed that the charge of the peak was practically independent of the SO_4^{2-} concentration. This suggests that the oxidation gave rise to a passivation of the electrode surface via the formation of a poorly soluble oxidation product, e.g. a neutral gold-sulfate complex. An analogous cathodic potential shift was also observed when increasing the KCl concentration (see Figure 3.11b). With the KCl concentration increasing from 0 to 10 µM, the anodic peak potential thus decreased from 0.565 V to 0.552 V. Finally, the peak size decreased and the peak became broader when the KCl concentration increased from 100 µM to 1 mM. A plot of the peak charge versus the KCl concentration for the oxidation peak also indicated a Langmuir-like dependence (see Figure 3.12) supporting the hypothesis involving the formation of a poorly soluble (and hence passivating) layer of a gold containing complex (or ion-pair) on the gold surface.

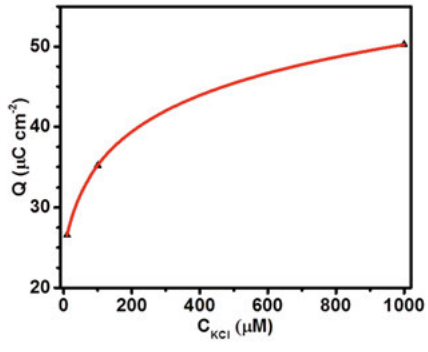

Figure 3.12. The peak charge density of the oxidation peak in the EDL region as a function of the KCl concentration: the black dots are the data points while the red solid line represents a Langmuir-type fit using the equation of y = 7.24 ln (x+29) yielding R^2=0.99997.

Furthermore, the reaction mechamism for the peak in the EDL region was investigated. First, experiments were conducted to demonstrate whether the reaction is a surface confined redox reaction or a diffusion controlled reaction. If the reaction is surface confined, the peak current should be proportional to ν, otherwise it should be proportional to $\nu^{1/2}$.[35] CV experiments were therefore carried out using a range of scan rates, i.e. 10, 25, 50, 75 and 100 mV/s in 50 mM H_2SO_4 solutions containing 0, 10, and 1000 µM

KCl. As can be seen in Figure 3.13, linear plots of the peak current (j) versus ν were obtained in all three cases indicating the presence of a surface confined redox reaction.

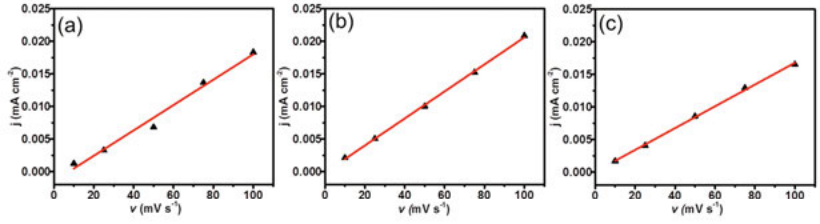

Figure 3.13. The oxidation peak current density as a function of vfor a KCl concentration of (a) 0 μM, (b) 10 μM and (c) 1000 μM in 50 mM H_2SO_4 solution. The black dots are the data points while the red solid lines represent linear fits to the data points.

Secondly, the valence of Au after oxidation in the EDL region was investigated. Usually, gold oxide formation (Au_2O_3) requires potentials above 1.1 V.[67] The peaks in the EDL region are therefore unlikely to be due to an oxidation of the gold electrode yielding Au(III). It is therefore proposed that the peaks seen in the EDL region are due to the formation of a passivating surface layer composed of Au(I) complexes with Cl^- or SO_4^{2-}. Here it should also be mentioned that large cathodic shifts in the redox potential compared to the standard potential can be observed when the metal ion concentration in the solution deviates greatly from 1.0 M (i.e. the concentration associated with the standard potential). Ag nanoparticles have hence been found to undergo oxidation at potentials about 0.4 V more negative than the Ag^+/Ag standard potential due to a low local concentration of Ag^+ caused by the fast diffusion of Ag^+ away from the silver nanoparticles [68]. In the present case, the local concentration of Au(I) may be decreased via the formation of poorly soluble complexes with Cl^- or SO_4^{2-}.

To confirm the formation of the Au(I) complexes with Cl^- or SO_4^{2-}, XPS has been performed on the gold electrodes scanned from 0 to 0.8 V in 50 mM H_2SO_4 solutions containing 10 μM or 1 mM KCl. The presence of the Cl and S on the Au surface has been confirmed and their dependence on the anion concentrations has been observed (see Figure 6 in ***Paper II***). However, it was difficult to detect a Au(I) peak, most likely due to the overlap with the signal due to metallic gold (not shown).

Based on the experimental findings, the oxidation peak observed in the EDL region is proposed to stem from a one-electron transfer gold oxidation process yielding a neutral Au(I)complex with Cl^- or SO_4^{2-}. The complexation with the ligand would then help to stabilize the Au(I) oxidation state and the voltammetric data also indicate that passivating layers of the complexes were formed on the gold surface. The proposed reaction can be illustrated using the equations below:

$$Au \rightarrow Au^{+} + e^{-} \qquad \text{Equation 3.1}$$

$$Au^{+} + Cl^{-} \rightarrow \left[AuCl\right]_{s} \qquad \text{Equation 3.2}$$

and

$$2Au^{+} + \left[SO_4^{2-}\right] \rightarrow \left[Au_2SO_4\right]_{s} \qquad \text{Equation 3.3}$$

Upon the formation of the complexes, the free concentration of Au(I) would decrease at the electrode surface which, according to the Nernst equation, would result in a cathodic shift in the redox potential, the magnitude of which would increase with increasing ligand concentration. The results further indicate that when KCl was added to the H_2SO_4 solution, the Au_2SO_4 on the electrode surface was gradually replaced by AuCl, as the peak potential was shifted in the negative direction.

Such oxidation peaks should hence always be expected when CV experiments are carried out in H_2SO_4 electrolytes and the peak shifts seen for these peaks with increasing cycle number may then be due to the increase of the concentration of the Cl^- leaking from the RE.

3.3. Practical guidelines for pretreating gold surfaces prior to functionalization

In this chapter, pretreatment methods to clean the microfabricated gold surface have been systematically characterized in terms of surface cleanliness, thiolated molecule binding and reproducibility. The investigated methods were (i) CV in H_2SO_4, (ii) KOH + H_2O_2 & LSV and (iii) O_2 plasma & ethanol. It was shown that all three methods significantly decreased the contamination and increased MCH surface coverage.

Most importantly, it was also revealed that surface pretreatment and characterization method, particularly CV in H_2SO_4, may induce structural changes to the gold surfaces due to the factors from the experimental setup. Accordingly, these alterations influence the characteristics of MCH functionalization. The factors include the leakage of Cl^- from the Ag/AgCl/sat. KCl RE as well as the dissolution and re-deposition of Pt from the Pt CE. Therefore, the use of the RE bridge to minimize the Cl^- leakage and avoid using the Pt CE are highly suggested. Moreover, as there may be poorly soluble Au(I) complexes formed on the gold surface during the CV in H_2SO_4, we also suggest to make sure the complexes have been reduced after the CV. Based on these findings, in the later experiments, we combined the "O_2 plasma & ethanol" and "CV in H_2SO_4" to pretreat and characterize the gold surface prior to the DNA immobilization. During the CV pretreatment, the RE bridge has been used and the big gold electrodes on the same chip (see section 2.1 for the electrode design) have been used as the CE.

4. Sensor characterization

4.1. DNA hybridization on the gold surface

The performance of electrochemical DNA biosensors is highly dependent on the target-probe DNA hybridization behaviors. With the negatively charged phosphate backbone and the relatively large size, the steric hindrance and the charge screening are two key factors determining the target-probe hybridization behavior. Usually, increasing the Γ_{Probe} could increase the steric hindrance, thus decreasing the hybridization efficiency. As the Γ_{Target} is determined by the Γ_{Probe} and the hybridization efficiency, to increase the Γ_{Target}, the Γ_{Probe} should be tailored. On the other hand, high salt concentration is favored for DNA hybridization. However, high salt concentration will reduce the λ_D and increase the charge screening effect, with should be avoided for potentiometric detection.

In this section, the target-probe DNA hybridization on the sensor surface and its dependence on the surface probe DNA coverage and the ionic strength were systematically investigated and quantified by surface plasmon resonance (SPR).

4.1.1. Tailoring the Γ_{Probe}

Currently, the most frequently used method to tailor the Γ_{Probe} is varying the probe DNA concentration in the solution for the electrode surface modification. Figure 4.1 shows the relationship of the probe DNA concentration and the Γ_{Probe} measured by CC and SPR. As is seen, when DNA concentration in the immobilized solution was lower than 100 nM (see the inset figure in Figure 4.1), the average Γ_{Probe} increased quasi-linearly (from $2.1 \pm 0.6 \times 10^{11}$ to $5.8 \pm 2.1 \times 10^{12}$ molecules cm^{-2} with increasing probe DNA concentration. The Γ_{Probe} reached it steady state at the probe concentration higher than 250 nM. The maximum Γ_{Probe} was $7.6 \pm 1.7 \times 10^{12}$ molecules cm^{-2} for CC measurements while it was $1.73 \pm 0.03 \times 10^{13}$ molecules cm^{-2} for SPR analysis. This deviation is probably due to the different gold surfaces (lab-fabricated gold electrodes for CC measurements and commercial SPR gold chips for SPR measurements).

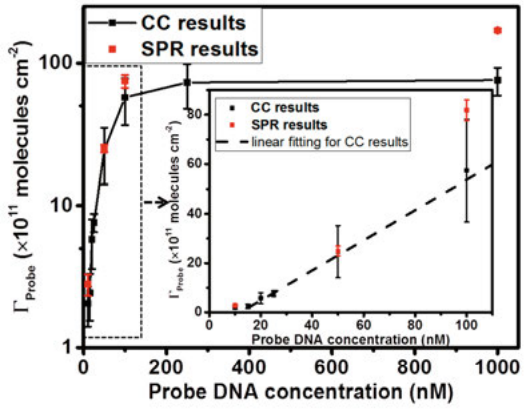

Figure 4.1. CC and SPR results of Γ_{probe} versus immobilized probe DNA concentration. Black dots and line: CC results; Red dot: SPR results. The inset figure shows the enlarged view of results at low probe DNA concentrations with linear scale. Each point depicts the average and standard deviations from 4 electrodes (or SPR sensorchip channels).

4.1.2. Relationship between the Γ_{Probe} and the target-probe DNA hybridization

The dependence of the probe-target hybridization on the Γ_{probe} was investigated. The hybridization experiments were conducted in the tris buffer (10 mM Tris-HCl, pH 7.4) with 1 M NaCl. Figure 4.2a shows the SPR analyses of surfaces with four different Γ_{Probe} (i.e., 1.49×10^{11}, 2.49×10^{12}, 7.82×10^{12}, and 1.70×10^{13} molecules/cm^2) after injecting 50 µl of 1 µM target DNA for ten minutes. As is seen in Figure 4.2a all the hybridization of probe-target increased and reached steady state within ten minutes of injection, and the maximum Γ_{Target} increased with increasing Γ_{probe}. Notably, the surface with the highest Γ_{Probe} had the slowest hybridization rate. The slow hybridization rate on the high Γ_{Probe} may be due to the large steric hindrance effects. In addition, the maximum hybridization efficiency decreased from 90 % to 22 % with increasing the Γ_{Probe} (Figure 4.2b).

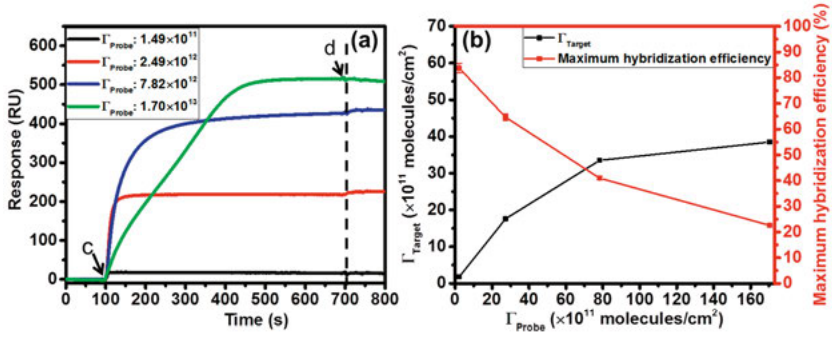

Figure 4.2. The influence of probe surface coverage density on the target hybridization. (a) The relationship of Γ_{Probe} on the hybridization response. At point c, 1 μM target DNA was injected; at point d, the injection was finished; (b) The influence of Γ_{Probe} on the Γ_{Target} and maximum hybridization efficiency. The running buffer and inject buffer was the tris buffer with 1 M NaCl. The flow rate was 5 μl per minute.

4.1.3. Relationship of ionic strength and the target-probe DNA hybridization

As illustrated above, lower ionic strength could reduce the probe-target hybridization efficiency due to the charge repulsion of the DNA phosphate backbone. This could be reflected by the melting temperature (T_m) of the probe-target duplexes at different salt concentrations [69]. To confirm this, the T_m of the DNA duplex was measured in the tris buffer with four different NaCl concentrations (1, 10, 100, 1000 mM). As shown in Table 4.1, both the measured T_m and the theoretical T_m decreased with decreasing NaCl concentration. It is worth noting that all the measured melting temperatures of the DNA duplexes are higher than room temperature (25 ˚C), which indicates the hybridization could take place at room temperature even at the lowest tested salt concentration. However, due to steric hindrance on the surface, the DNA hybridization behavior could be quite different comparing to that in the bulk solution [12]. Therefore, the hybridization behavior of the probe-target DNA on the surface versus the NaCl concentration was also investigated.

Table 4.1 T_m versus NaCl concentration in the tris buffer.

NaCl concentration (mM)	Measured T_m (˚C)	$Theoretical T_m (˚C)
1000	-*	78.5
100	66	61.9
10	48	45.3
1	45#	28.7

*The T_m could not be measured due to too high salt concentration that has an impact on PicoGree fluorescence.
#The large deviation between the measured T_m and theoretical T_m may be due to the presence of 10 mM tris.
$The theoretical T_m was calculated using nearest neighbor method using OligoCalc calculator.[70]

Figure 4.3 shows the SPR results of the probe-target hybridization on gold surfaces in the buffer solutions with different NaCl concentrations. Generally, it can be seen that the probe-target hybridization rate decreased with decreasing NaCl concentration for all the surfaces. Moreover, low salt concentration had stronger influence on the hybridization occurring on the surface with higher Γ_{Probe}. When the salt concentration was reduced to 10 mM and 1 mM, the hybridization efficiency decreased remarkably for all the surfaces and none of the surfaces could reach steady state, even with 15 minutes' injection time. Notably, almost no hybridization was registered on the surface with 1.70×10^{13} molecules/cm in 10 mM NaCl, even though the target concentration was increased from 1 μM to 3 μM for this surface (Figure 4.3a). The hybridization also became invisible for the other 3 surfaces with lower Γ_{Probe} when the NaCl concentration was reduced to 1 mM (Figure 4.3b-d). Although T_m results suggest the hybridization could take place in the low salt buffer, the deviation between the results of SPR and T_m analysis confirmed the difference of the DNA hybridization in the bulk solution and on the surface, due to the extra steric hindrance effect on the latter.

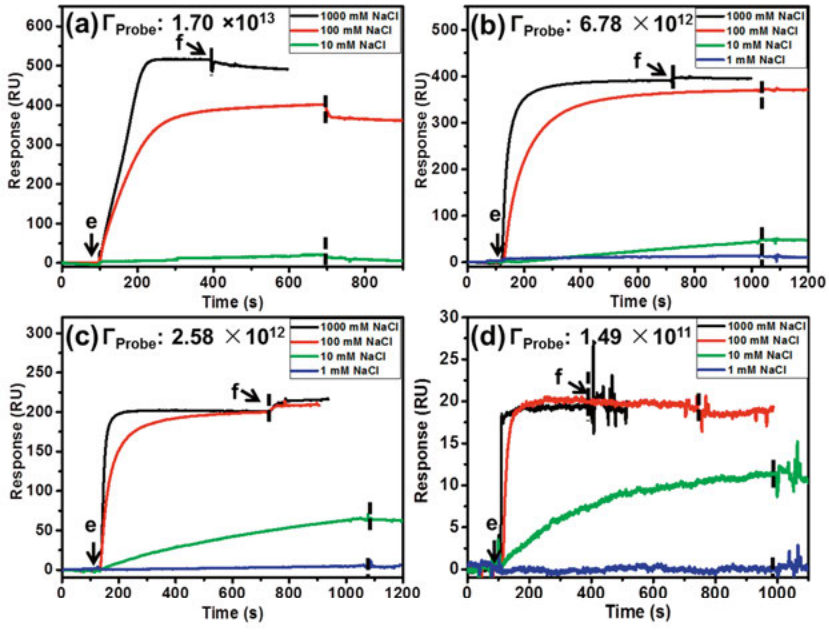

Figure 4.3. The SPR response of the gold surfaces immobilized with the Γ_{Probe} of (a) 1.70 $\times 10^{13}$; (b) 6.78$\times 10^{12}$; (c) 2.58 $\times 10^{12}$, and (d) 1.49 $\times$ 10^{11}, molecules cm^{-2} versus different NaCl concentrations. At point e, either 3μM for for (a) or 1 μM for (b), (c) and (d) target was injected. At point f and after the dashed line, the injection was finished. The flow rate was 5 μl per minute.

4.2. Potentiometric detection of DNA

The potentiometric signal of the ISFET based DNA sensor is generated by the additional surface charge induced within the λ_D by the hybridized target DNA molecules [11,27,28]. As illustrated in last section, the hybridized target DNA amount is determined by the Γ_{Probe} and their hybridization efficiency. The hybridization efficiency decreased significantly with increased Γ_{Probe}, due to the steric hindrance [71,72]. On the other hand, λ_D is determined by the ionic strength [32]. Lower ionic strength could yield larger λ_D to benefit the signal [73]. However, due to the charge repelling on the DNA phosphate backbone, lower ionic strength could also reduce the probe-target hybridization efficiency. In this section, the trade-off for Γ_{Probe} and ionic strength has been investigated to estimate the theoretical potentiometric signal. The potentiometric detection of DNA was also performed. The estimated results and the measured results were compared.

4.2.1. Estimation of the potentiometric signal for DNA detection

4.2.1.1. Estimation of the potentiometric signal for DNA detection with diluting buffer method

Firstly, the potentiometric signal for the results in Figure 4.3 was estimated. In the estimation, we simply assume that potentiometric signal is the surface potential change ($\Delta\varphi$) caused by the net surface charge induced by the hybridized target DNA (Q_h) charging up C_{DL} [74]. It is again noted that only the charge within the λ_D can contribute to the net surface charge. Therefore,

$$\Delta\varphi = \frac{Q_h}{C_{DL}} \qquad \text{Equation 4.1}$$

Where, C_{DL} is around 2 μF cm^{-2} in the tris buffer for a DNA/MCH modified gold surface as measured by CC (See Table 4.2). It is also known that each nucleotide in the DNA chain contains one negative charge [33]. So the amount of Q_h is determined by the number of nucleotides within λ_D ($N_{nucleotide}$).

Table 4.2. The typical values for C_{DL} measured CC in 10 mM tris buffer. ΔE=-0.35 V

Q_{DL} (μC cm^{-2})	$C_{DL}=Q_{DL}/\Delta E$ (μF/cm^2)
0.72	2.05
0.65	1.87
0.67	1.93
0.47	1.30
0.69	1.96

λ_D in the tris buffer solutions with 1 to 1000 mM NaCl was calculated and listed in Table 4.3. $N_{nucleotide}$ was calculated after subtracting the length of linker (around 1 nm) from λ_D, given the distance between two neighboring bases is 0.34 nm (for dsDNA) and assuming the DNA molecules stand on the surface (Table 4.3). Note that no side interactions on the sensing electrode, such as surface protonation/deprotonation which could buffer the DNA signal, nor the DNA conformation change, were considered in the estimation. The estimated amount should thus be the upper limit of the signal generation.

The estimation of the potentiometric signal is also summarized in Table 4.3. For all the conditions with the salt concentration higher than 100 mM, no DNA nucleotide is located within λ_D, resulting in no detectable charge. This indicates that the ISFET could not be applied directly in physiological solutions (ionic strength at 200-300 mM) with λ_D about 0.8 nm [73]. In the tris buffer with 10 mM or 1 mM NaCl, no potential change could be registered for the surface with highest Γ_{Probe} (i.e., 1.70 $\times 10^{13}$ molecules cm^{-2}) since no hybridization took place under this condition. The largest potentiometric signal was estimated to be 121 ± 5 mV, with Γ_{Probe} of 2.58 × 10^{12}

molecules cm^{-2} and in the tris buffer with 10 mM NaCl. Besides, as the hybridization efficiency was significantly decreased in the tris buffer with 1 mM NaCl, the estimated potentiometric signal in this salt concentration was small (around 10 mV).

Table 4.3. Estimation of the potentiometric signals for different Γ_{Probe} and salt concentrations.

Γ_{probe} (molecules/cm^2)	C_{NaCl} (mM)	λ_D (nm)	$N_{nucleotide}$ within λ_D	$^*\Gamma_{Target}$ (molecules/cm^2)	$^*Q_h$ (C cm^{-2})	$^*\Delta\varphi$ (mV)
1.70×10^{13}	1000	0.30	0	$3.85 \pm 0.04 \times10^{12}$	0	0
	100	0.92	0	$2.85 \pm 0.03 \times10^{12}$	0	0
	10	2.14	3	$-0.04 \pm 0.01\times10^{12}$	0	0
	1	2.90	5	-	-	-
6.78×10^{12}	1000	0.30	0	$3.08 \pm 0.08\times10^{12}$	0	0
	100	0.92	0	$2.93 \pm 0.04\times10^{12}$	0	0
	10	2.14	3	$3.68 \pm 0.17\times10^{11}$	$1.77 \pm 0.08\times10^{-7}$	88 ±4
	1	2.90	5	$3.35 \pm 1.88\times10^{10}$	$2.68 \pm 1.50\times10^{-8}$	13 ± 8
2.58×10^{12}	1000	0.30	0	$1.52 \pm 0.16\times10^{12}$	0	0
	100	0.92	0	$1.53 \pm 0.11\times10^{12}$	0	0
	10	2.14	3	$5.04 \pm 0.20\times10^{11}$	$2.42 \pm 0.10\times10^{-7}$	121 ± 5
	1	2.90	5	$2.76 \pm 1.18\times10^{10}$	$2.21 \pm 0.95\times10^{-8}$	11 ± 5
1.49×10^{11}	1000	0.30	0	$1.44 \pm 0.03 \times10^{11}$	0	
	100	0.92	0	$1.46 \pm 0.04 \times10^{11}$	0	
	10	2.14	3	$8.86 \pm 0.65 \times10^{10}$	$4.26 \pm 0.31 \times10^{-8}$	21 ± 2
	1	2.90	5	$2.76 \pm 0.88 \times10^{10}$	$2.21\pm0.71 \times10^{-8}$	11 ± 4

*The results contain the mean and the standard deviations. The standard deviation was calculated from 3 to 4 measurements.

The sensitivity of the surface with Γ_{Probe} of 2.58×10^{12} molecules cm^{-2} and in the tris buffer with 10 mM NaCl was further investigated. **Figure 4.4** shows the SPR results and the corresponding estimated potentiometric signals of the probe-target hybridization on this surface with different target concentrations. It can be seen that Γ_{Target} and the corresponding estimated potentiometric signal decreased with reduced target concentration. The estimated potentiometric signal from 100 nM target concentration was only 10 mV. Assuming the intrinsic potential fluctuation of RE is 1 mV [75], considering the signal-to-noise ratio (STN > 3), this indicates the lower detection limit of this method is about 30 nM with 3 mV potentiometric signal. Notably, these estimations assume no side interfacial interactions are taking place, thus this is in the ideal case. Therefore, reported signals higher than these estimations should be carefully evaluated.

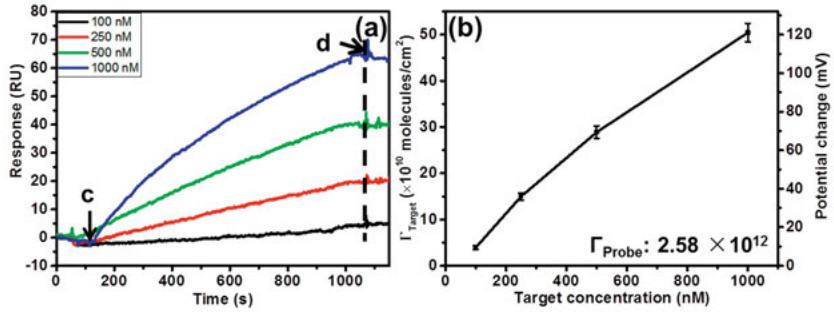

Figure 4.4. The calibration curve for probe-target hybridization in the tris buffer solution with 10 mM NaCl and on the surface with the probe coverage of 2.58×10^{12} molecules cm^{-2}. (a) The SPR results. At point c, the target was injected; at point d and after dashed line, the injection was stopped. Due to the slow hybridization rate, the injection time was 15 minutes. The flow rate was 5 µM per minute. (b) The target coverage and the estimated potential change versus target concentration. The indicated error bars denote the standard deviations based on 3 to 4 measurements.

4.2.1.2. Estimation of potentiometric detection signal for DNA detection with an alternative method

The major reason for the low potential signal with diluting buffer method is the contradicting requirements of salt concentration for hybridization and charge registration (i.e., λ_D). An alternative method is to separate these two processes to different buffer solutions: hybridization at high salt concentration followed by potentiometric measurement at low salt concentration. Since a prerequisite for this alternative method is that the hybridized DNA duplex is stable in the low salt buffer, the stability of DNA duplexes in the tris buffer with different NaCl concentrations has been examined (See Figure 4.5).

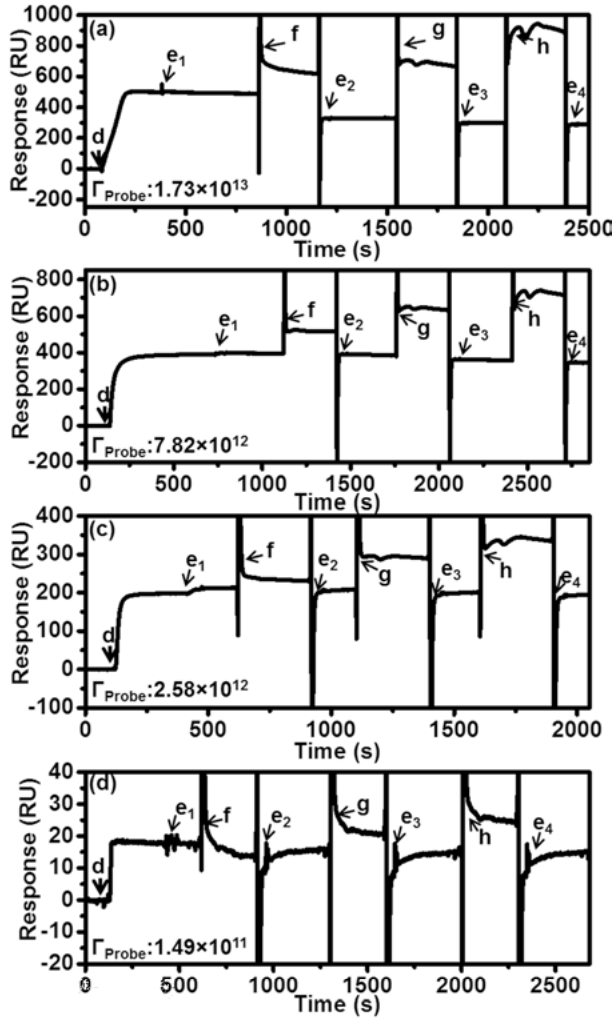

Figure 4.5. The SPR results of the stability of DNA duplexes in the tris buffer containing different concentrations of NaCl on the gold surfaces with the probe coverage of (a) 1.73×10^{13} molecules cm^{-2}; (b) 7.82×10^{12} molecules cm^{-2}; (c) 2.58×10^{12} molecules cm^{-2}; and (d) 1.49×10^{11} molecules cm^{-2}. In all the figures, at point d, 3 μM (for a) or 1 μM (for b, c and d) of target DNA was injected; at point e, the injection was stopped and the running buffer flowed, the subject numbers depict the different times of stopping injection; at point f, the tris buffer containing 100 mM NaCl was injected for 5 minutes; at point g, the 10 mM tris containing 10 mM NaCl was injected for 5 minutes; at point h, the 10 mM tris buffer containing 1 mM NaCl was injected for 5 minutes. The flow rate was 5 μl per minute.

As seen from Figure 4.5a for the surface with highest Γ_{Probe}, after the target was injected for 200 s, the SPR response reached steady state (maximum). After the target injection was stopped at e_1, the response change was 490 RU, corresponding to the Γ_{Target} at 3.86×10^{12} molecules cm^{-2}. After 5

minutes' injection of buffer containing 100 mM, 10 mM and 1 mM NaCl, the SPR response decreased to 289 RU, corresponding to a Γ_{Target} of 2.28×10^{12} molecules cm^{-2}, suggesting 60% of the target was remaining in tris buffer with 1 mM NaCl. Specifically, on the surface with Γ_{Probe} of 7.82×10^{12} molecules cm^{-2}, the SPR response after hybridization was 420 RU. The 5 minutes' injections of the tris buffer containing 100 mM, 10 mM and 1 mM NaCl yielded 336 RU(Figure 4.5b), corresponding to a final Γ_{Target} of 2.65×10^{12} molecules cm^{-2} (80 % target remained). On the surfaces with the Γ_{Target} of 2.58×10^{12} molecules cm^{-2} and 1.49×10^{11} molecules cm^{-2} (Figure 4.5c and 4.5d), after injecting the buffers with 1mM NaCl, 91 % and 95 % of the target remained. The corresponding remaining Γ_{Target} were 1.53×10^{12} and 1.45×10^{11} molecules cm^{-2}.

As the results show, the surface the Γ_{Probe} of 7.82×10^{12} molecules cm^{-2} had the most remaining targets after the washing with low salt buffer. The corresponding potentiometric signal in the tris buffer with 1 mM NaCl was estimated to be 1059 mV. Furthermore, the SPR analysis has been conducted for estimating the potentiometric signals for different target concentrations using the alternative methods. The SPR analysis is shown in Figure 4.6a. The resulting Γ_{Target} after hybridizing in the tris buffer with 1 M NaCl as well as the estimated potentiometric signal at 1 mM NaCl are shown in Figure 4.6b. It can be observed that with decreasing the target concentration, the hybridization rate decreased. When the target concentration decreased from 1000 nM to 10 nM, the Γ_{Target} decreased from $3.36 \pm 0.03\times10^{12}$ molecules cm^{-2} to $1.60 \pm 0.02\times10^{11}$ molecules cm^{-2}, corresponding to potentiometric signal changing from 1074 ± 10 mV to 51 ± 6 mV. Provided that the intrinsic potential fluctuation of the RE is about 1 mV, the lower detection limit with the proposed alternative method is around 0.6 nM for 3 mV (STN > 3) potentiometric signal.

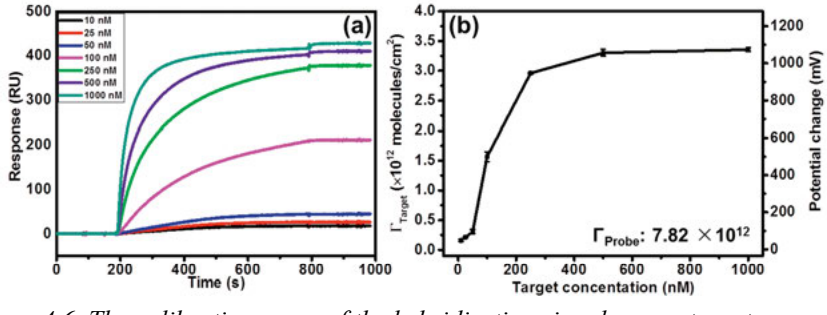

Figure 4.6. The calibration curve of the hybridization signal versus target concentration. (a) The SPR response of the surface immobilized with 100 nM probe to different target concentrations. The sample buffer and running buffer was tris buffer with 1 M NaCl. (b) The as-hybridized target coverage and the estimated potentiometric change versus the target concentration.

4.2.2 Potentiometric detection of DNA with gold coated -SiNW-FET

In the last section, we have estimated the detection limits of potentiometric DNA sensors using SPR analyses without considering the side reactions occurring on the sensing interface. Herein, the potentiometric detection of the DNA was performed with the gold coated SiNW-FET. The SiNW-FET has a n-channel. The detailed information for SiNW-FET and the measurement setup could be found in section 2.4.6. The gold surface was functionalized with probe DNA and MCH as the sensing layer. 100 nM of probe DNA was used for immobilization, which could yield a Γ_{Probe} of around 5.8×10^{12} molecules/cm^2 (Figure 4.1).

As the estimation in Section 4.2.1 shows, with the method of diluting buffer, the maximum potentiometric signal could be obtained occurring in the tris buffer containing 10 mM NaCl. Therefore, potentiometric detection of DNA was first performed in this buffer (Figure 4.7). In principle, the hybridized target DNA could introduce additional negative charge on the gold surface, thus increasing the V_T of the SiNW-FET. As seen in Figure 4.7, the V_T drifted initially and after the ΔV_T was stabilized, 10, 100, and 1000 nM target DNA in was injected successively. However, the injection of target DNA even upto 1 μM target concentration did not change the V_T. The measurements were repeated on four different SiNW-FETs. None of them could register the shift in V_T caused by the DNA hybridization.

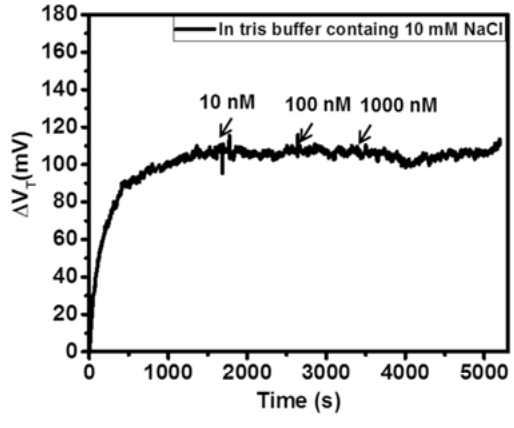

Figure 4.7. Real-time potentiometric detection of DNA in the tris buffer containing 10 mM NaCl. The injected target concentration was 10 nM, 100 nM and 1000 nM. The flow rate was 5 μl/min. For each injection, the time is around 15 minutes.

The potentiometric DNA detection with the alternative method, i.e., DNA hybridization in the tris buffer containing 1M NaCl and measurement in the tris buffer containing 1mM NaCl, was also demonstrated. As different salt concentrations were used for hybridization and for the charge registration, it

is important to know the influence of the high salt concentration buffer on the potentiometric signal registered in the low salt concentrations buffer (Figure 4.8a). As can be seen in the Figure 4.8ai, the tris buffer containing 1mM NaCl and the buffer containing 1 M NaCl were injected alternatively. The difference of the ΔV_T in the buffer with 1 mM NaCl was calculated before and after the injection of 1 M NaCl buffer, yielding the ΔV_T of -39, -20, and -16 mV, respectively. The measurement on the MCH modified device on the same chip exhibited a similar decrease of the ΔV_T (see Figure 4.8aii) after injecting the tris buffer containing 1 M NaCl. The differential ΔV_T was obtained by subtracting the change in Figure 4.8aii from 4.8ai. The yielded differential ΔV_T before and after three times of injection of the tris buffer with 1 M NaCl was around -20, -3, and -3 mV, respectively. Since the noise level of the measurement was upto 2 mV, with STN>3, only the potential change above 6 mV could be registered reliably. This suggests the influence of using different buffer for the measurement could be eliminated by repeating the injections and using the differential signal.

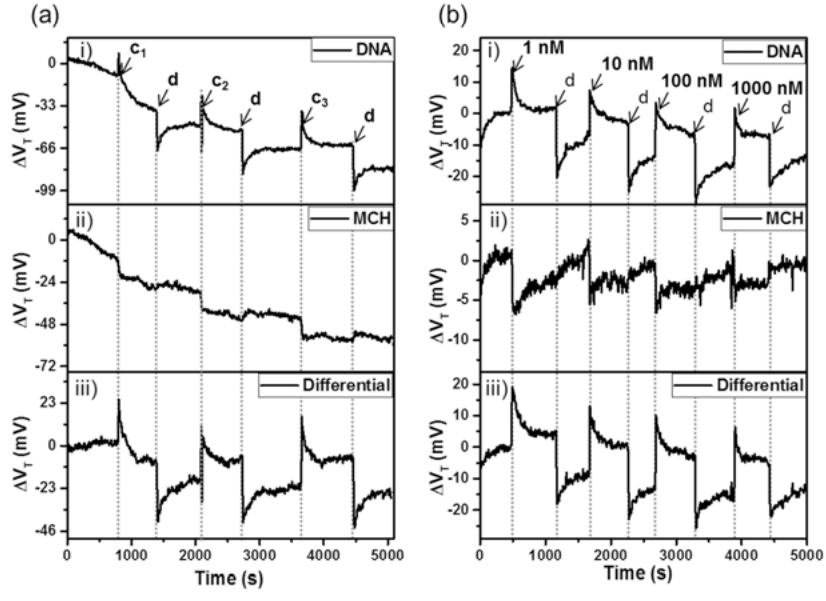

Figure 4.8. (a) Real-time potentiometric measurement to study the influence of 1 M NaCl; At point c, the tris buffer containing 1 M NaCl was injected for 10 minutes, the subscript numbers represent for different runs; at point d, the tris buffer containing 1 mM NaCl was injected. (b) The real-time potentiometric measurement of DNA hybridization with the alternative method. This measurement was performed immediately after (a).

The potentiometric detection of DNA was performed immediately after the differential ΔV_T caused by injection of 1 M NaCl was eliminated. The real-time response after injecting 1, 10, 100, and 1000 nM target DNA was shown in Figure 4.8b. The registered differential ΔV_T in the tris buffer con-

taining 1 mM NaCl after the injections of different concentration of target DNA was -8, -13, -13, and -13 mV. Moreover, as the SiNW-FET used in this study is n-channel FET, the DNA hybridization should introduce more negative charge on the surface, thus increasing the V_T. The negative ΔV_T may come from the drift of the system. The result suggests no ΔV_T could be registered with increasing the target DNA concentration. This experiment was repeated on six different SiNW-FETs. However, the results were similar as the results shown in Figure 4.8b, suggesting no potentiometric signal could be generated by DNA hybridization.

4.2.3. The limitations in the potentiometric DNA detection

Although the estimation based on the SPR analysis suggests the DNA hybridization can be registered by potentiometric methods, the experimental results suggest that the potentiometric DNA detection with the gold-coated SiNW-FET is not a feasible method. As the estimation did not take the side interactions occurring on the sensing interface into consideration, the results of the real-time potentiometric measurements suggest these side interactions may overwhelm the potentiometric signal induced by DNA hybridization.

Indeed, many factors could decrease the potentiometric signal caused by DNA hybridization. In the estimation, it is assumed that all the negative charge on the DNA within the λ_D could be registered. Actually, the charge on the DNA could be shielded or neutralized to a great extent by the counter-ions in the solution [33]. According to Manning's counter-ion condensation theory, upto 76 % of the negative charge on the DNA could be shielded by monovalent cations [76]. Therefore, this counter-ion condensation effect can reduce the expected hybridization signal and prevent successful measurements.

Moreover, the pH buffering effects on the surface could be another factor accounting for the decrease of potentiometric signal. The study on protein modified FET shows, the pH sensitivity on the surface could buffer the potential change based on Donnan equilibrium [77]. In this study, the author proposed that if the ISFET shows a Nernstian behavior, no potentiometric signal could be caused by proteins adsorbed in the membrane on the gate of an ISFET. Besides, studies on the potentiometric detection of Ca^{2+} shows competing reactions occurring on the surface could reduce the potentiometric signal [78]. In this study, the pH sensitivity of the gold surface was also found could reduce the sensitivity of Ca^{2+}. The pH sensitivity of the probe DNA/MCH modified gold surface was demonstrated (see Figure 4.9a). As seen in Figure 4.9a, the pH sensitivity of the gold, MCH modified gold, and the probe DNA/MCH modified gold was 10.7 ± 1.8, 34.9 ± 2.8, and 20.1 ± 1.4 mV/pH. This result confirms the pH sensitivity of the sensing interface could be another factor decreasing the potentiometric detection signal of DNA hybridization.

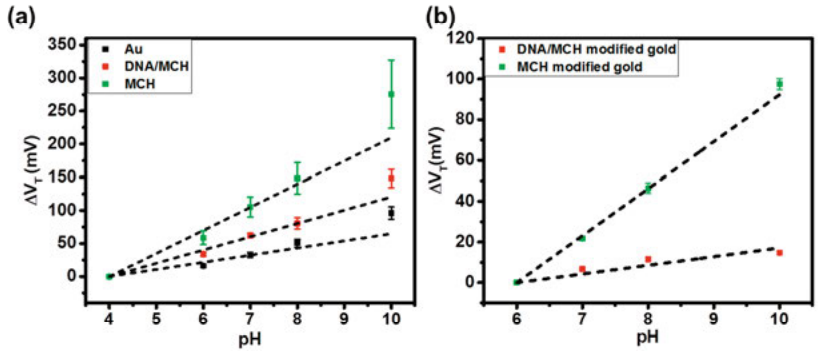

Figure 4.9. (a) The pH sensitivity results of the gold, MCH modified gold, and probe DNA/MCH modified gold; (b) The pH sensitivity of probe DNA/MCH modified gold in the presence of 100 μM ferri- and ferrocyanide. The indicated error bars denote the standard deviations based on five different measurements.

In addition, since there is no fixed couple presenting on the gold surface, gold could directly sense the change occurring in the bulk solution. This suggests that the potential of the buffer solution may dominate the gold sensing potential. To confirm this, the pH sensitivity of the MCH and the probe DNA/MCH modified gold surface in the presence of ferri- and ferrocyanide was investigated (Figure 4.9b). As expected, the pH sensitivity of both the MCH and the probe DNA/MCH modified surface decreased to 23.1 ± 0.9 and 4.3 ± 0.8 mV/pH.

Finally, the STN and the DNA conformational change before and after DNA hybridization could also limit the potentiometric detection signal of DNA hybridization.

4.3. EIS analysis of DNA hybridization on DNA aptamer/MCH modified gold

DNA aptamers are synthetic oligonucleotides that can adopt secondary or tertiary structures after binding to certain targets with extremely high specificity [44]. Owing to the highly specific affinity of aptamers to target molecules, aptamers have been adopted as the recognition probes in the development of ultrasensitive biosensors [44,79]. Recently, target- induced strand displacement (TISD) has been proposed to increase the sensitivity and selectivity of aptamer sensors [80,81]. By introducing a short-length probe DNA, which can hybridize with a partial aptamer, the conformational change of an aptamer can be enhanced after the target displaces the probe thanks to the different flexibility of the ssDNA and dsDNA [82]. To achieve a sensitive and selective aptamer with the TISD method, the requisite is that the aptamer can hybridize with the probe efficiently. Importantly, the hybrid-

ization of the aptamer-probe DNA is supposed to induce a significant and reproducible signal change to enable a large detection signal when the target displaces the probe.

In this section, EIS analysis of DNA hybridization was studied on the aptamer/MCH SAM modified gold surfaces, combined with ferri- and ferrocyanide (i.e. $Fe(CN)_6^{3-}$ and $Fe(CN)_6^{4-}$) as redox-active mediators. A DNA aptamer with 38 bases and a short sequence probe DNA (P1) were used. The drift issues within this system are studied. The importance of a stable and reproducible interface is demonstrated and addressed.

4.3.1. Irreproducible EIS results for aptamer/MCH modified gold electrodes after hybridization with P1

The EIS measurements were performed prior to and after aptamer/P1 hybridization on the aptamer/MCH modified gold electrodes. As mentioned in Section 2.3.2.2, during the hybridization, the aptamer/MCH modified gold electrode was incubated in the 95 ˚C buffer with P1. During the incubation with P1, the solution slowly cooled to room temperature and the hybridization took place. To differentiate these data from the results shown later in the text, the EIS results obtained immediately after aptamer/MCH modification and after hybridization with P1 were marked with “first cycle”. The results of the faradaic EIS measurements following the hybridization with P1 on the aptamer/MCH mixed SAM modified gold were, however, not reproducible. Figure 4.10a and 4.10b show the results of the EIS measurements for two electrodes, before and after the P1 hybridization. Note that the diameter of the semicircle, i.e., the R_{CT}, in the Nyquist plot decreased slightly after the hybridization for one electrode while it increased for the other electrode.

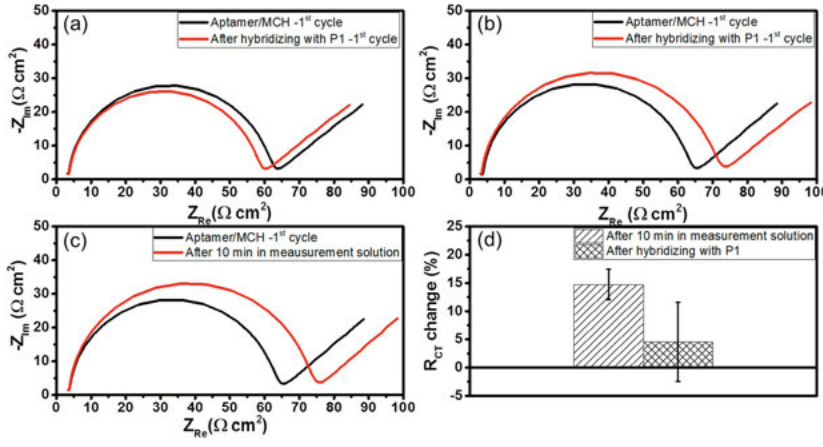

Figure 4.10. Faradaic EIS analyses of aptamer/MCH modified gold electrodes in the binding buffer solution containing ferri- and ferrocyanide at room temperature. (a, b) The first cycle EIS results of two independent measurements for aptamer/MCH modified gold electrodes before and after hybridization with P1; (c) The first cycle EIS results for the aptamer/MCH electrodes after ten minutes of incubation in the measurement solution; (d) R_{CT} changes after hybridization with P1, and after ten minutes of incubation in measurement solution, respectively. The R_{CT} values were obtained by fitting the results to the Randles cell equivalent circuit model. The R_{CT} changes were then calculated as $(R_{CT,\ after}-R_{CT,\ initial})/R_{CT,\ initial}\times 100\%$. The indicated error bars denote the standard deviations based on six different electrodes.

As illustrated in 1.4.3, R_{CT} changes induced by the hybridization of target DNA can be either positive or negative, which is dependent on not only the accumulation of additional negative charges on the surface but also by the physical blocking of the access of the redox molecules to the electrode surface [12]. More negative charge should be present on the surface after the aptamer-P1 hybridization, which could result in an increased repulsion of the negatively charged ferri- and ferrocyanide complexes. This should result in an increase in R_{CT}. However, the conformation changes of the aptamer after hybridization with P1 could decrease the R_{CT} [10]. As illustrated in section 1.3.3, the extent of conformation change after hybridization is dependent on the surface coverage. Given a similar coverage measured by CC, i.e. $9.2 \pm 0.9 \times 10^{11}$ molecules cm^{-2} of the aptamer on the different electrodes in this study, the aptamer should undergo similar conformational change after the hybridization. Analogous R_{CT} changes should therefore be seen for the electrodes. The irreproducible changes after P1 hybridization here indicate that either the surface conformations of aptamer varied between two electrodes or the surface was not stable during the measurements.

Moreover, when carrying out repeated faradaic EIS measurements on the aptamer/MCH mixed SAM modified gold electrode after ten minutes of incubation in the measurement solution, an additional increase in R_{CT} was

observed (Figure 4.10c). This suggests that the irreproducible results for the aptamer/MCH modified gold electrodes prior to and after the P1 hybridization in Figure 4.10 could be caused by the R_{CT} drift.

The reproducibility issue on the R_{CT} change after the hybridization and after the incubation in the measurement solution was statistically studied on six different electrodes. The obtained average change in R_{CT} showed that the R_{CT} increased after the hybridization with P1 while the uncertainty in the average change was significant (see Figure 4.10d). A student's t-test based on the results in Figure 4.10 d showed that there was no significant difference between the R_{CT} changes caused by the hybridization with P1 and those seen during the subsequent measurements. This clearly made it difficult to determine whether the increase in R_{CT} was caused by random variations, drift or the hybridization process.

4.3.2. Drift in R_{CT} and C_{DL} for aptamer/MCH modified gold electrodes

To get a better understanding of the drift in R_{CT} for aptamer/MCH modified gold electrodes, the faradaic EIS measurements were carried out for 18 hours to investigate whether the system would reach a stable state or not. As the results in Figure 4.11 show, the EIS measurements need roughly 12 hours to be stabilized. During the stabilization, R_{CT} and C_{DL} both increased.

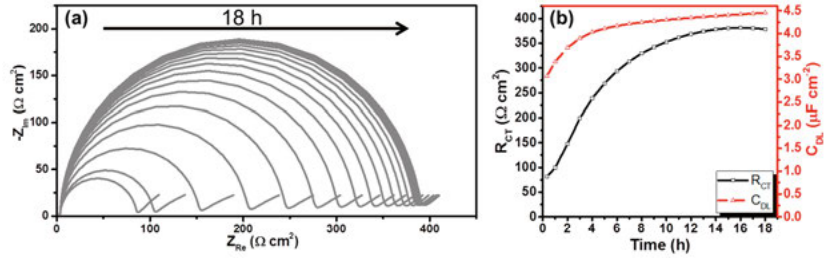

Figure 4.11. Faradaic impedance drift for an aptamer/MCH electrode in the binding buffer solution containing 10 mM ferri and ferrocyanide during continuous measurement at room temperature. (a) Nyquist plots for different times with a one-hour interval between two measurements; (b) The extracted R_{CT} and C_{DL} values versus time.

It has previously been reported that repeated measurements can give rise to an increase in R_{CT}.[37] However, this explanation was excluded with the experiments. Comparable increases in R_{CT} were observed for the electrodes with and without repeated measurements during conditioning in the measurement solution (see details in ***Paper IV*** and Figure S5 in the Supporting information). It is reasonable to assume that the drift in R_{CT} and C_{DL} was caused by some changes taking place on the electrode surface upon the incubation in the measurement solution.

4.3.3 Faradaic EIS analyses on aptamer/MCH modified gold after hybridization and after stabilization

After the faradaic EIS measurements for the aptamer/MCH modified gold stabilized, the stabilized R_{CT} was evaluated. The electrode was then washed and incubated in the 95 ˚C binding buffer solution either in the absence or presence of P1 for 1 hour. The solutions were initially at 95 ˚C and then cooled down to room temperature during the incubation process. Finally, the electrodes were washed and the faradaic EIS measurements were performed. A gradual increase in R_{CT} was also seen for the electrode after the hybridization with P1 or after incubation in the hot buffer (See Figure S6 in ***Paper IV***). The stabilized R_{CT} value was then taken as the R_{CT} value for the hybridized electrode. In Figure 4.12a and 4.12b, the stabilized R_{CT} values obtained for the aptamer/MCH electrode prior to and after incubating in the hot buffer with and without P1 were compared. Moreover, the statistics on six different electrodes for each experiment show, the R_{CT} increase was 30 ± 10% for the former (with P1) and was 112 ± 12% for the latter (i.e., without P1). Since a Student's t-test showed the difference between the R_{CT} values obtained in the presence and absence of P1 hybridization was significant at the 95% level, it is immediately clear that the change in R_{CT} was not only caused by the hybridization. Moreover, the results indicate that the increase in R_{CT} due to the increased temperature actually was larger than the change seen in the presence of the hybridization.

This is surprising as it would be assumed that the main change in the R_{CT} value should be due to the hybridization. As the experimental results demonstrate that the changes in R_{CT} depend on both the hybridization reaction and the temperature, it would hence not be straightforward to employ the present sensing protocol. This suggests that hybridizations in hot buffer solutions either should be avoided or that results obtained with the present protocol should be verified using another approach prior to use. From a fundamental point of view, it is clearly important to identify the reasons for the large changes seen in R_{CT} when changing the temperature. This issue is therefore discussed in the next section.

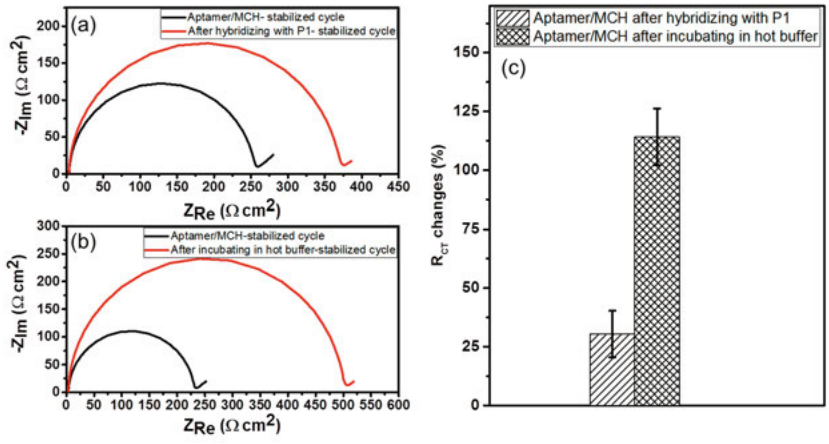

Figure 4.12. Stabilized faradaic EIS results for (a) an aptamer/MCH modified gold electrode before and after hybridization with P1, (b) an aptamer/MCH modified gold before and after incubation in the hot binding buffer solution. (c) R_{CT} changes obtained after hybridization with P1 and incubation in the hot binding buffer, respectively. The R_{CT} values were obtained from fits of the data to the Randles equivalent circuit for six electrodes and the R_{CT} changes were calculated as $(R_{CT,\ after}-R_{CT,\ initial})/R_{CT,\ initial}\times 100\%$. The error bars denote the STD calculated based on the data from six electrodes. The EIS measurements were conducted at room temperature.

4.3.4. Reasons for R_{CT} and C_{DL} drift for aptamer/MCH modified electrodes

Many authors have attributed drift in R_{CT} to interactions between ferri- and ferrocyanide complexes and gold electrodes [38,39]. They proposed that the drift due to cyanides, which were released from the ferri- and ferrocyanide, could etch gold. As the cyanide etching should decrease the R_{CT}, which is different from the trend observed here, the cyanide etching could not be the reason for the R_{CT} drift here. A detailed discussion on this can be found in ***Paper IV***. It can consequently be concluded that there must be another reason for the drift seen in the EIS results for the present aptamer/MCH modified gold electrodes. As the same buffer was used for the whole process and no water rinse and no nitrogen blow was applied, no other factors from the measurement or preparation could account for the R_{CT} drift. Since a SAM passivated gold surface is a "high resistance surface", the reorganization defects in the SAM may influence the EIS signal significantly via the creation of "routes" for the ferri- and ferrocyanide molecules [20,83]. Therefore, it is reasonable to think the R_{CT} drift comes from some structure change involving defect redistribution on the aptamer/MCH SAM.

4.3.3.1. R_{CT} and C_{DL} drift of MCH modified gold electrodes prior to hybridization

To identify the origin of the drift in R_{CT} and C_{DL}, one first needs to determine whether the drift is caused by structural changes induced by the aptamer or the MCH. Intuitively, it would be straightforward to attribute the R_{CT} and C_{DL} drift to a gradual structural change of the aptamer due to the fact that the latter is a flexible and charged molecule. However, the long-time EIS analysis on the MCH modified gold electrode showed the same drift pattern as on the aptamer/MCH modified gold electrodes (see Figure 4.13). This suggests the faradaic impedance drift for the aptamer/MCH modified electrode was dominated by the change in the MCH SAM, probably due to a gradual reorganization of the MCH SAM.

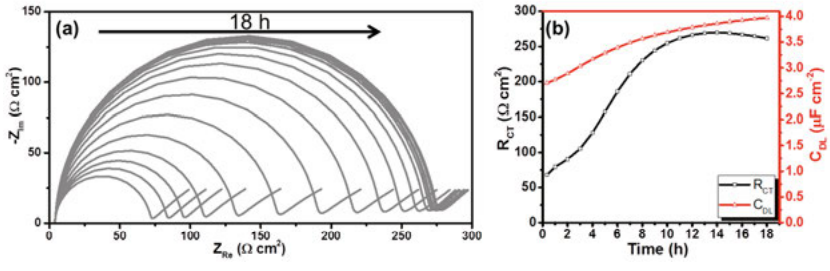

Figure 4.13. Faradaic EIS drift for a MCH modified gold electrode in the binding buffer solution containing 10 mM ferri- and ferrocyanides. (a) Nyquist plots recorded at different times; (b) The extracted R_{CT} and C_{DL} as a function of the time.

While the increase in R_{CT} can be explained based on a reorganization of the MCH layer yielding a more close-packed layer (with fewer defects) the results also indicate that this likewise gives rise to an increase in the C_{DL} values. Since the increase in R_{CT} indicates that the access to the gold surface area decreased during the reorganization, it is reasonable to assume the increase in the C_{DL} values also was a result of the MCH layer becoming thinner (and more compact) during the reorganization.

4.3.3.2. R_{CT} changes for aptamer/MCH modified electrodes after incubation in hot binding buffer

After figuring out that the R_{CT} and C_{DL} drift seen for the aptamer/MCH modified gold electrode prior to hybridization was due to the reorganization of the MCH SAM, the reason for the impedance drift after incubation in hot binding buffer was investigated. The question is whether this drift was also from the MCH reorganization. Figure 4.14 and 15 depict the faradaic EIS drift for aptamer/MCH and MCH modified gold electrodes found after incubation in the hot binding buffer. The R_{CT} first increased and then stabilized after 22 hours for both the aptamer/MCH and MCH modified gold electrodes (Figure 4.14 and 4.15). It has been reported that high temperature annealing could cause SAM reorganization [84]. The longer times required for the

stabilization suggest that the exposure to the hot buffer result in a larger disturbance on the structure of the aptamer/MCH SAM, which needed a longer time to be stabilized.

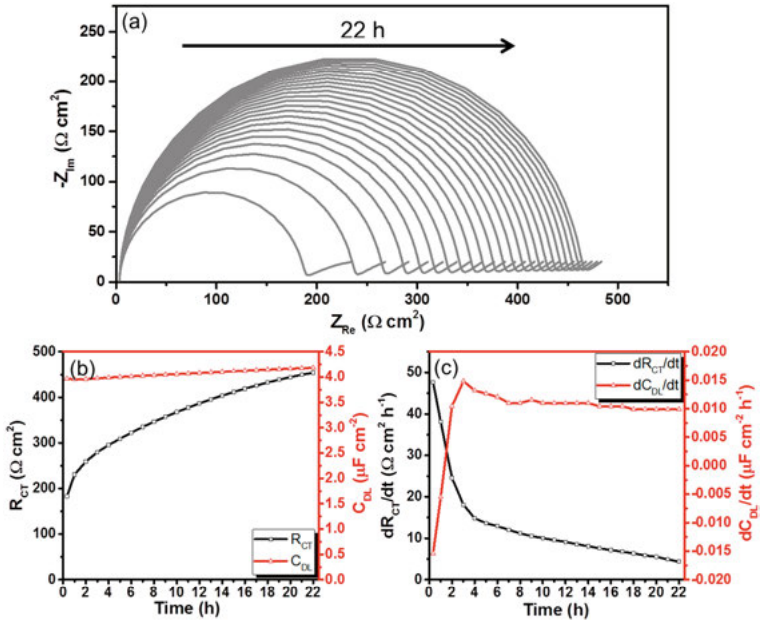

Figure 4.14. Faradaic EIS signal drift for an aptamer/MCH modified gold electrode after incubation in the hot hybridization buffer. (a) Nyquist plots. The time interval between two line was one hour; (b) The evaluated R_{CT} and C_{DL} values as a function of time; (c) The R_{CT} and C_{DL} change rates versus time. The EIS measurements were conducted at room temperature in the buffer solution containing 10 mM ferri- and ferrocyanide.

The C_{DL} and R_{CT} drift patterns for the aptamer/MCH and MCH modified gold electrodes were then closely examined. First, it can be observed that both aptamer/MCH and MCH modified gold experienced the gradual structure change during the EIS measurements after incubation in the hot binding buffer and the MCH structure change still dominated the R_{CT} drift. The slight differences in the C_{DL} drift (i.e., the different drift rates for aptamer/MCH and MCH modified gold electrodes) suggests the structure change of the aptamer also contributed to the impedance drift.

These two hypotheses could be further supported by the statistical comparison of the R_{CT} increases induced by the hot buffer on the aptamer/MCH and MCH modified electrode. The statistics on six electrodes show that the R_{CT} increased 91 ± 10 % on MCH modified gold after incubation in the hot binding buffer. As mentioned earlier, the R_{CT} increased 112 ± 12 % for the aptamer/MCH modified gold after incubation in the hot binding buffer. This further confirmed that the change in R_{CT} seen for the aptamer/MCH modified gold electrodes likewise was dominated by the reorganization of the

MCH induced by the hot buffer. Additionally, the structure change of the aptamer, e.g. involving an unfolding of some aptamers, should account for this difference of R_{CT} change.

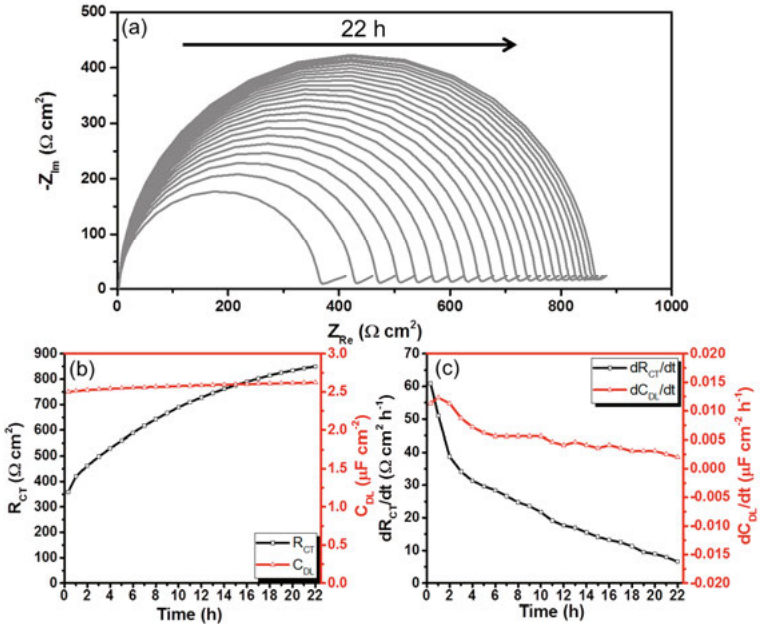

Figure 4.15. Faradaic EIS signal drift for a MCH modified gold electrode after incubation in the hot hybridization buffer. (a) Nyquist plots; (b) The evaluated R_{CT} and C_{DL} values as a function of time; (c) The R_{CT} and C_{DL} change rates versus time. The EIS measurements were conducted at room temperature in the buffer solution containing 10 mM ferri- and ferrocyanide.

4.3.5. Importance of stabilization process on hybridization signal

After identifying the main reason for the R_{CT} and C_{DL} drift prior to and after hybridization, the influence of the stabilization step on the hybridization signal should be discussed further. This can be done using a modified Randles equivalent circuit and a simplified physical model of the aptamer/MCH functionalized gold surface. As indicated in Figure 4.16, this modified equivalent circuit included three current branches where C_{DL} represents the double layer capacitance (incorporated with the aptamer/MCH SAM), while $R_{CT,apt}$ and $R_{CT,MCH}$ denote the R_{CT} at the aptamer and MCH SAM sites, respectively. Ideally, the change in R_{CT} should only be due to the aptamer-P1 hybridization (i.e., a change in $R_{CT,apt}$). As discussed above, there may, however, also be a change in R_{CT} due to the reorganization of the MCH SAM (i.e., a change in $R_{CT,MCH}$) in which case the measured R_{CT} change would be affected by both $R_{CT,apt}$ and $R_{CT,MCH}$ (i.e. $R_{CT,apt}*R_{CT,MCH}/(R_{CT,apt}+R_{CT,MCH})$). As the R_{CT} drift prior to hybridization was

dominated by the MCH, we can know $R_{CT,MCH}$ is smaller than $R_{CT,apt}$. In this case, $R_{CT,MCH}$ would therefore determine the R_{CT} value and the change in $R_{CT,apt}$ would remain invisible. After the stabilization, the $R_{CT,MCH}$ increased. As a result, the $R_{CT,apt}$ change would become visible. Given the significant difference between the changes in R_{CT} due to the hybridization and the hot buffer exposure, it can be inferred that the $R_{CT,apt}$ and $R_{CT,MCH}$ values should have been similar after the stabilization as the changes in both $R_{CT,apt}$ and $R_{CT,MCH}$ were able to contribute to the measured R_{CT} changes at this point.

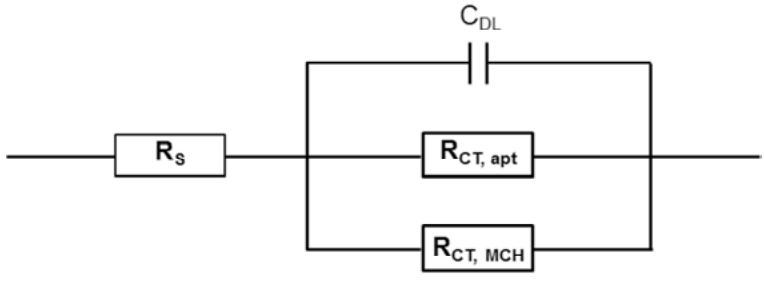

Figure 4.16. (a) A modified Randles equivalent circuit in which $R_{CT,apt}$ represents the R_{CT} for the aptamer coated surface while $R_{CT,MCH}$ represents the R_{CT} for the MCH modified surface.

5. Summary

As illustrated in Chapter 1, many interface-related factors can influence the performance of gold-based electrochemical DNA sensors. This thesis focuses on a comprehensive investigation of these factors and provides practical guidelines for the development of gold-based electrochemical DNA sensors. The major findings of this thesis are summarized as follow:

1. Contamination on gold electrodes induced during the microfabrication process could block binding sites for the subsequent surface functionalization. Three pretreatment methods for cleaning gold surfaces, (i) CV in dilute H_2SO_4, (ii) gentle basic piranha incubation followed by linear sweep voltammetry in dilute KOH, and (iii) oxygen plasma treatment followed by incubation in ethanol, are systematically investigated and compared regarding the gold surface cleanliness and thiolated molecule binding. All three methods significantly decrease the contamination and increased MCH surface coverage. In addition, surface pretreatment and characterization methods, particularly CV in H_2SO_4, may induce structural changes to the gold surface.

2. Factors from the experimental setup are responsible for the structural change of the gold surfaces prepared by CV in H_2SO_4. Cl^- leakage from the Ag/AgCl/sat. KCl RE is responsible for the poor reproducibility in the gold Ox/Re region as the result of the etching and subsequent re-deposition of the dissolved gold. Platinum dissolving from the platinum CE and depositing on the gold WE gives rise to an increased catalytic behavior with respect to the HER/HOR. Quantitative analysis reveals that the ratio between the dissolved gold and platinum concentrations depends on the Cl^- concentration. The surface ratio between the co-deposited platinum and gold rather than the absolute amount of the deposited platinum on the gold electrode determines the HER catalytic performance. In addition, the origin of the redox peaks seen in the EDL region has been ascribed to the formation and decomposition of Au(I) chloride and sulfate complexes.

3. The hybridization of probe-target DNA is strongly dependent on Γ_{Probe} and salt concentrations. The probe-target hybridization rates and efficiency decreased with decreasing salt concentrations. Moreover, a low salt concentration has a stronger influence on the hybridization occurring on a surface with higher Γ_{Probe}. Therefore, for a smart design of a DNA modified surface aimed at DNA detection, the choice of Γ_{Probe} and salt concentration should be carefully considered.

4. Lowering the salt concentration could increase λ_D, thus resulting in more registered charges on the DNA. However, due to the contradicting requirements regarding the salt concentration for the hybridization and charge registration, the potentiometric signal generated by DNA hybridization with diluting buffer methods is very weak according to our estimation based on the SPR results. An alternative method could be to separate these two processes, i.e., performing DNA hybridization in a high salt concentration buffer and conducting the potentiometric measurement in a low salt concentration buffer. This could increase the potentiometric signal theoretically.

5. Many factors can limit the potentiometric signal induced by DNA hybridization using the gold-coated SiNW FET, resulting in no potentiometric signal. First, the negative charge could be shielded by the counterions in the solution. The pH buffering effect of the sensing interface could be another factor that limits the potentiometric signal generated by DNA hybridization. Besides, the communication between the gold and the electrolyte, the conformational change of DNA before and after hybridization, and the noise should also influence the potentiometric signal.

6. The EIS measurements on aptamer/MCH SAM modified gold surfaces exhibited significant drift. This drift strongly affects the reproducibility of the EIS signal from the aptamer-target hybridization. As a result, no significant difference between R_{CT} changes induced by the aptamer-target DNA hybridization and the 10 minutes' incubation in the measurement solution. A long time conditioning of the aptamer/MCH modified electrode in the measurement solution is required to reach a stable R_{CT} baseline prior to the aptamer-probe DNA hybridization. The MCH SAM on the gold surface reorganization could be responsible for the drift during the EIS measurements. The hot buffer used during the aptamer-P1 hybridization aimed at increasing DNA hybridization efficiency could induce additional MCH and aptamer reorganization, and thus further drift in R_{CT}. Therefore, it is suggested that the use of high temperature in the EIS measurement should be carefully evaluated or avoided.

Sammanfattning på svenska

Guldbaserade etikettfria elektrokemiska DNA-sensorer har studerats i stor omfattning för diagnostik av biomarkörer. Känsligheten och reproducerbarheten hos dessa sensorer bestäms av avkänningsgränssnittet: för de DNA-modifierade guldytorna. Denna avhandling studerar systematiskt processerna för att preparera DNA-sensorgränssnitten såväl som deras effekter på sensorns prestanda. De viktigaste resultaten i avhandlingen sammanfattas enligt följande:

1. Föroreningar på guldelektroder som uppstår vid mikrofabrikationsprocessen kan blockera bindningar för efterföljande ytfunktionalisering. Tre behandlingsmetoder för rengöring av guldytor, (i) cyklisk voltammetri (CV) i H_2SO_4, (ii) mild basisk piranha-inkubation följt av linjär svep-voltammetri i utspädd KOH och (iii) syrgasplasmabehandling följt av inkubation i etanol, har systematiskt undersökts och jämförts beträffande guldytans renhet och tiolers molekylbindning. Alla tre metoderna minskade föroreningarna signifikant och ökade ytbeläggningen av MCH. Dessutom kan behandlingsmetoder och karakteriseringsmetoder, särskilt CV i H_2SO_4, inducera strukturella förändringar av guldytan.

2. Faktorer från experimentuppställningen ger upphov till den strukturella förändringen av guldytorna framställda med CV i H_2SO_4. Cl-läckage från Ag/AgCl/sat. KCl-referenselektroden ger upphov till den dåliga reproducerbarheten i guld Ox/Re-området som ett resultat av etsningen och efterföljande återdeponeringen av det upplösta guldet. Platina som upplöses från motelektroden av platina och som deponeras på den guldelektroden ger upphov till ett förstärkt katalytiskt beteende med avseende på HER/HOR. Kvantitativ analys visar att förhållandet mellan koncentrationen av upplöst guld och platina beror på Cl-koncentrationen. Ytförhållandet mellan det samdeponerade platinat och guldet, snarare än den absoluta mängden av deponerat platina på guldelektroden, bestämmer den katalytiska prestandan för HER. Dessutom har ursprunget till redoxtopparna som kan ses i EDL-regionen tillskrivits bildandet och sönderdelningen av Au(I) klorid och sulfatkomplex.

3. Hybridiseringen av prob-bitar av DNA är starkt beroende av probens täckningdensitet (Γ_{Probe}) och saltkoncentrationer. Prob-bitens hybridiseringsgrad och effektivitet minskade med minskande saltkoncentrationer. Dessutom har en låg saltkoncentration en starkare inverkan på hybridiseringen som sker på en yta med högre Γ_{Probe}. Därför bör valet av Γ_{Probe} och saltkoncentrat-

ion noga övervägas för en smart design av en DNA-modifierad yta som ska användas för DNA-detektering.

4. En sänkning av saltkoncentrationen kan öka Debye-längden (λ_D), vilket leder till fler registrerade laddningar på DNA:t. På grund av de motstridiga kraven på saltkoncentrationen för hybridisering och laddningsregistrering är emellertid den potentiometriska signalen som genereras av DNA-hybridisering med utspädande buffertmetoder mycket svag enligt vår uppskattning som baseras på ytplasmon-analys. Ett alternativt förfarande skulle kunna vara att separera dessa två processer, d.v.s. genomföra DNA-hybridisering i en buffert med hög saltkoncentration och utföra den potentiometriska mätningen i en buffert med låg saltkoncentration. Detta skulle teoretiskt kunna öka den potentiometriska signalen.

5. Många faktorer kan begränsa den potentiometriska signalen som induceras av DNA-hybridisering med användning av guldbelagd SiNW FET förutom Γ_{Probe} och saltkoncentrationen. I första hand kan växelverkan mellan guldytan och elektrolyten orsaka drift och fluktuationer i bakgrundsnivån för potentialen, vilket resulterar i osynlighet för den potentiometriska signalen vid DNA-hybridisering. Dessutom kan pH-känsligheten för den DNA/merkaptohexanol (MCH) modifierade guldytan vara en annan faktor som begränsar den potentiometriska signalen. Tillsats av ferri- och ferrocyanid i mätbuffertlösningen kan stabilisera bakgrundsnivån för potentialen och minska pH-känsligheten för den DNA/MCH-modifierade ytan medan den också kan buffra den potentiometriska signalen från DNA-hybridisering.

6. De elektrokemiska impedansspektroskopimätningarna (EIS) på aptamer/MCH SAM-modifierade guldytor uppvisade betydande drift. Denna drift påverkar starkt reproducerbarheten hos EIS-signalen från aptamer-target hybridiseringen. Resultatet blir att det inte finns någon signifikant skillnad mellan R_{CT}-förändringar som inducerats av aptamer-target DNA-hybridisering och av den 10 minuter långa inkubationen i mätlösningen. En lång tidskonditionering av den aptamer/MCH-modifierade elektroden i mätlösningen krävs för att nå en stabil R_{CT} bakgrundsnivå innan aptamer-prob DNA-hybridiseringen. Omstruktureringen av MCH SAM på guldytan kan ge upphov till drift under EIS-mätningarna. Den varma bufferten som användes under aptamer-P1-hybridiseringen och som syftade till att öka DNA-hybridiseringseffektiviteten skulle kunna inducera ytterligare omstrukturering av MCH och aptamer och därmed ytterligare drift hos R_{CT}. Därför föreslås att nyttjandet av hög temperatur vid EIS-mätningen noggrant bör utvärderas eller undvikas.

Acknowledgement

Thank you, Zhen Zhang, for letting me be a Ph.D student at Uppsala. Thanks for being so patient to me during my studies. We learned and made process in electrochemistry and the solid-electrolyte interface together. I am very impressed by your eager to new knowledge, your sense of logic, and good presentation ability.

Thank you, Shi-Li Zhang, for being my co-supervisor. I am very impressed by your carefulness and preciseness in physics, mathematics, and languages, as well as your passion for science.

Thank you, Leif Nyholm, for being my unofficial co-supervisor. You are a so nice, knowledgeable and serious scientist. I do not know how hard it would be without your guidance in my study and without your encouragement when I was upset with my results. I feel so lucky to meet you in Sweden.

Thank you, Asta Makaravičiūtė as my co-worker and friend. This thesis is not only mine but also yours. I really enjoy the time working together with you. I learned a lot from you, regarding knowledge, writing, and attitude to research. I am very appreciated for your comfort when I was stressed and your regards even after you left the group.

Thank you, Helena Danielson and Eldar Abdurakhmanov, for being my collaborators during my last year. I am very appreciated for your kind help and fruitful discussions. Thank you, Martin Sjödin, for your help and discussions in the QCM measurement. Thank you, Jean Pettersson for the help of ICP-MS.

Thank you, Tomas Nyberg, for translating my thesis summary to Swedish and I enjoy the time working with for PT01. Thank you, Tomas Kubert and Amit Patel, for teaching me PT01 and helping me solve problems.

Thank you, Jonathan Scragg for screening my thesis and giving me useful and encouraging comments.

Thank you, Qitao Hu, Yingtao Yu and Si Chen for providing me the SiNW-FET, teaching me about the measurement and helping me debug the problems for my last project. Besides, thank you Yingtao for your hard work. I knew you were busy with your own project but every time I tried to push you, you never said “no” to me. Moreover, thank you, Qitao Hu, for being my good friends and good teacher. I enjoy the good time spending with you, such as conversations, travels, experiments, etc.

Thank you, Rimantas Brucas, Farahad Zamany, Stefan Nygren, Örjan Vallin, Victoria Sternhagen and Sven Norén for your kind help in the cleanroom.
Thank you Shuangshuang Zeng, Chenyu Wen, Shiyu Li for being good colleagues and friends. Thanks for all the kind help and good conversions. I could not point everything because we share many forgetful experiences. Thank my current and former group members, Da Zhang, Quentin Palomar, Lukas Jablonka, Yuan Zhu, Yifei Liu, Elis Nycander, Indrek Must and Nathan Netzer, for the collaborations and any help. Thank you, my great colleagues in FTE, Yi Ren, Man Song, Long Hoang Duc, Wei-Chao Chen, Syaiful Redzwan, Renbin Tong, Sven Englund, Yupeng Yang, Yao Yao, Ngan Pham, Libo Chen, Zhibin Zhang, Suyi Li, Malkolm Hinnemo, Patrik Ahlberg, Imran Aziz, Fredrik Larsson, Robin Augustine, Dragos Dancila, Marika Edoff, Carl Hägglund, Jan Keller, Faraz Khavari, Jörgen Olsson, Charlotte Platzer Björkman, , Katharina Rudisch, Siddharth Sourabh Sahu, Nishant Saini, Nina Shariati Nilsson, Tobias Törndahl, Villamayor, Michelle Marie, etc.
Thank you, Huan Wang, for being my close friend. We shared happiness, sorrows, exercises and lunches. Thank you for all the moments. Thank you, Jie Zhao, for being my good friends and good roommate. Thank you my great corridor friends, XueYing Kong, Rui Sun, Shenyang Zhou, Peng Zhang and Lulu Wu for all the help and the happy talks. Thank you, Lei Tian, Mingzhi Jiao, Yuanyuan Han, Dan Wu, Zhen Hua Liu, Litao Yin, YuKai Huang, Tianbo Wu, Zhaohui Wang, Hu Li, Zhigang Chai, Haidong Liu, Wenjuan Liu, and Shujiang Wang for being my friend in the Angstrom. Thank you, Lars Riekehr, Adam Hultqvist, Björn Landeke-Wilsmark, Hasan Ali, Federico Cantoni, for being my cleanroom friends.
Thank you, Ramy Salameh for your administrative help.
Thank you Chiao-Wei Tseng for all the snacks you put on my desk when I worked late and the ginger tea when I felt cold. You are one of the most serious scientists I have ever met. Thank you Xi Chen and Pianpian Wu for all the good shares and thank you Xi Chen for teaching me swim. Thank you, Qinghua Liao, for helping me open the door at BMC. Thank you, Yiming Chen, for being good friends and all the encouragements. Thank you, Ruijun Pan and Qiuhong Wang, for being my great neighbors in Flogsta.
Thank you, Ye Zou, Qian Liu, KaiChung, Jing Chen, Chenyu Wang, Adrian, and Anil for being my badminton friends. Thank you, Kun Wei, for offering me living place in the first year and all the good suggestions.
最后，谢谢我的爸爸和哥哥在我博士期间对我的鼓励，谢谢你们在我低落时的安慰，谢谢做我坚强的后盾。谢谢我在天堂中的妈妈对我从小到大无微不至的照顾，我会带着您对我的期盼走下去。

References

[1] N. Arroyo-Currás, P. Dauphin-Ducharme, G. Ortega, K.L. Ploense, T.E. Kippin, K.W. Plaxco, Subsecond-Resolved Molecular Measurements in the Living Body Using Chronoamperometrically Interrogated Aptamer-Based Sensors, ACS Sens. 3 (2018).

[2] K. Brown, M. McMenemy, M. Palmer, M.J. Baker, D.W. Robinson, P. Allan, L. Dennany, Utilization of an Electrochemiluminescence Sensor for Atropine Determination in Complex Matrices, Anal. Chem. 91 (2019) 12369–12376.

[3] S.J. Smith, C.R. Nemr, S.O. Kelley, Chemistry-Driven Approaches for Ultrasensitive Nucleic Acid Detection, J. Am. Chem. Soc. 139 (2017) 1020–1028.

[4] S.O. Kelley, Advancing Ultrasensitive Molecular and Cellular Analysis Methods to Speed and Simplify the Diagnosis of Disease, Acc. Chem. Res. 50 (2017) 503–507.

[5] D. Grieshaber, R. MacKenzie, J. Vörös, E. Reimhult, Electrochemical Biosensors - Sensor Principles and Architectures, Sensors. 8 (2008) 1400–1458.

[6] Y. Wu, R.D. Tilley, J.J. Gooding, Challenges and Solutions in Developing Ultrasensitive Biosensors, J. Am. Chem. Soc. 141 (2019) 1162–1170.

[7] D. Wei, M.J. A. Bailey, P. Andrew, T. Ryhänen, Electrochemical biosensors at the nanoscale, Lab. Chip. 9 (2009) 2123–2131.

[8] M. Cui, Y. Wang, H. Wang, Y. Wu, X. Luo, A label-free electrochemical DNA biosensor for breast cancer marker BRCA1 based on self-assembled antifouling peptide monolayer, Sens. Actuators B Chem. 244 (2017) 742–749.

[9] P. Dauphin-Ducharme, K.W. Plaxco, Maximizing the Signal Gain of Electrochemical-DNA Sensors, Anal. Chem. 88 (2016) 11654–11662.

[10] M. Gębala, W. Schuhmann, Controlled Orientation of DNA in a Binary SAM as a Key for the Successful Determination of DNA Hybridization by Means of Electrochemical Impedance Spectroscopy, ChemPhysChem. 11, 2887–2895.

[11] B. M. Lowe, K. Sun, I. Zeimpekis, C.-K. Skylaris, N. G. Green, Field-effect sensors – from pH sensing to biosensing: sensitivity enhancement using streptavidin–biotin as a model system, Analyst. 142 (2017) 4173–4200.

[12] M. Gebala, W. Schuhmann, Understanding properties of electrified interfaces as a prerequisite for label-free DNA hybridization detection, Phys. Chem. Chem. Phys. 14 (2012) 14933–14942.

[13] J.J. Gooding, Electrochemical DNA Hybridization Biosensors, Electroanalysis. 14 (2002) 1149–1156.

[14] A label-free DNA sensor based on impedance spectroscopy, Electrochimica Acta. 53 (2008) 7467–7474.

[15] A. Gao, N. Lu, Y. Wang, P. Dai, T. Li, X. Gao, Y. Wang, C. Fan, Enhanced Sensing of Nucleic Acids with Silicon Nanowire Field Effect Transistor Biosensors, Nano Lett. 12 (2012) 5262–5268.

[16] C. Vericat, M. E. Vela, G. Benitez, P. Carro, R. C. Salvarezza, Self-assembled monolayers of thiols and dithiols on gold : new challenges for a well-known system, Chem. Soc. Rev. 39 (2010) 1805–1834.
[17] J.C. Love, L.A. Estroff, J.K. Kriebel, R.G. Nuzzo, G.M. Whitesides, Self-Assembled Monolayers of Thiolates on Metals as a Form of Nanotechnology, Chem. Rev. 105 (2005) 1103–1170.
[18] T. Doneux, A. de Ghellinck, E. Triffaux, N. Brouette, M. Sferrazza, C. Buess-Herman, Electron Transfer Across an Antifouling Mercapto-hepta(ethylene glycol) Self-Assembled Monolayer, J. Phys. Chem. C. 120 (2016) 15915–15922.
[19] J. Chen, B. Chang, S. Oyola-Reynoso, Z. Wang, M. Thuo, Quantifying Gauche Defects and Phase Evolution in Self-Assembled Monolayers through Sessile Drops, ACS Omega. 2 (2017) 2072–2084.
[20] P. Diao, M. Guo, R. Tong, Characterization of defects in the formation process of self-assembled thiol monolayers by electrochemical impedance spectroscopy, J. Electroanal. Chem. 495 (2001) 98–105.
[21] Q. Guo, F. Li, Self-assembled alkanethiol monolayers on gold surfaces: resolving the complex structure at the interface by STM, Phys. Chem. Chem. Phys. 16 (2014) 19074–19090.
[22] G.E. Poirier, E.D. Pylant, J.M. White, Crystalline structures of pristine and hydrated mercaptohexanol self-assembled monolayers on Au(111), J. Chem. Phys. 104 (1996) 7325–7328.
[23] J. Fuchs, J.-B. Fiche, A. Buhot, R. Calemczuk, T. Livache, Salt Concentration Effects on Equilibrium Melting Curves from DNA Microarrays, Biophys. J. 99 (2010) 1886–1895.
[24] J.R. Wenner, M.C. Williams, I. Rouzina, V.A. Bloomfield, Salt dependence of the elasticity and overstretching transition of single DNA molecules., Biophys. J. 82 (2002) 3160–3169.
[25] C.J. Burden, Y. Pittelkow, S.R. Wilson, Adsorption models of hybridization and post-hybridization behaviour on oligonucleotide microarrays, J. Phys. Condens. Matter. 18 (2006) 5545.
[26] B. Tinland, A. Pluen, J. Sturm, G. Weill, Persistence Length of Single-Stranded DNA, Macromolecules. 30 (1997) 5763–5765.
[27] T.S. Bronder, A. Poghossian, S. Scheja, C. Wu, M. Keusgen, D. Mewes, M.J. Schöning, DNA Immobilization and Hybridization Detection by the Intrinsic Molecular Charge Using Capacitive Field-Effect Sensors Modified with a Charged Weak Polyelectrolyte Layer, (2015).
[28] M.O. Noor, U.J. Krull, Silicon nanowires as field-effect transducers for biosensor development: A review, Anal. Chim. Acta. 825 (2014) 1–25.
[29] T.S. Bronder, A. Poghossian, S. Scheja, C. Wu, M. Keusgen, D. Mewes, M.J. Schöning, DNA Immobilization and Hybridization Detection by the Intrinsic Molecular Charge Using Capacitive Field-Effect Sensors Modified with a Charged Weak Polyelectrolyte Layer, ACS Appl. Mater. Interfaces. 7 (2015) 20068–20075.
[30] C.-J. Chu, C.-S. Yeh, C.-K. Liao, L.-C. Tsai, C.-M. Huang, H.-Y. Lin, J.-J. Shyue, Y.-T. Chen, C.-D. Chen, Improving Nanowire Sensing Capability by Electrical Field Alignment of Surface Probing Molecules, Nano Lett. 13 (2013) 2564–2569.
[31] P. Bergveld, Thirty years of ISFETOLOGY: What happened in the past 30 years and what may happen in the next 30 years, Sens. Actuators B Chem. 88 (2003) 1–20.

[32] M. Braus, The theory of electrolytes. I. Freezing point depression and related phenomena (Translation), (2019).
[33] A. Poghossian, A. Cherstvy, S. Ingebrandt, A. Offenhäusser, M.J. Schöning, Possibilities and limitations of label-free detection of DNA hybridization with field-effect-based devices, Sens. Actuators B Chem. 111–112 (2005) 470–480.
[34] A. Lasia, Electrochemical impedance spectroscopy and its applications, in: Mod. Asp. Electrochem., Springer, 2002: pp. 143–248.
[35] A.J. Bard, L.R. Faulkner, J. Leddy, C.G. Zoski, Electrochemical methods: fundamentals and applications, wiley New York, 1980.
[36] B.L. Garrote, A. Santos, P.R. Bueno, Perspectives on and Precautions for the Uses of Electric Spectroscopic Methods in Label-free Biosensing Applications, ACS Sens. 4 (2019) 2216–2227.
[37] A. Bogomolova, E. Komarova, K. Reber, T. Gerasimov, O. Yavuz, S. Bhatt, M. Aldissi, Challenges of Electrochemical Impedance Spectroscopy in Protein Biosensing, Anal. Chem. 81 (2009) 3944–3949.
[38] J. Lazar, C. Schnelting, E. Slavcheva, U. Schnakenberg, Hampering of the Stability of Gold Electrodes by Ferri-/Ferrocyanide Redox Couple Electrolytes during Electrochemical Impedance Spectroscopy, Anal. Chem. 88 (2016) 682–687.
[39] S. Vogt, Q. Su, C. Gutiérrez-Sánchez, G. Nöll, Critical View on Electrochemical Impedance Spectroscopy Using the Ferri/Ferrocyanide Redox Couple at Gold Electrodes, Anal. Chem. 88 (2016) 4383–4390.
[40] L.M. Fischer, M. Tenje, A.R. Heiskanen, N. Masuda, J. Castillo, A. Bentien, J. Émneus, M.H. Jakobsen, A. Boisen, Gold cleaning methods for electrochemical detection applications, Microelectron. Eng. 86 (2009) 1282–1285.
[41] R.F. Carvalhal, R. Sanches Freire, L.T. Kubota, Polycrystalline Gold Electrodes: A Comparative Study of Pretreatment Procedures Used for Cleaning and Thiol Self-Assembly Monolayer Formation, Electroanalysis. 17 (2005) 1251–1259.
[42] S. Trasatti, O.A. Petrii, Real surface area measurements in electrochemistry, J. Electroanal. Chem. 327 (1992) 353–376..
[43] A. Kick, M. Bönsch, K. Kummer, D.V. Vyalikh, S.L. Molodtsov, M. Mertig, Controlling structural properties of self-assembled oligonucleotide–mercaptohexanol monolayers, J. Electron Spectrosc. Relat. Phenom. 172 (2009) 36–41.
[44] A.B. Iliuk, L. Hu, W.A. Tao, Aptamer in Bioanalytical Applications, Anal. Chem. 83 (2011) 4440–4452.
[45] A.B. Steel, T.M. Herne, M.J. Tarlov, Electrochemical Quantitation of DNA Immobilized on Gold, Anal. Chem. 70 (1998) 4670–4677.
[46] A. Einstein, Zur Elektrodynamik bewegter Körper, Ann. Phys. 322 (1905) 891–921.
[47] A. Fahlman, K. Hamrin, J. Hedman, R. Nordberg, C. Nordling, K. Siegbahn, Electron Spectroscopy and Chemical Binding, Nature. 210 (1966) 4–8.
[48] A. Hamelin, Cyclic voltammetry at gold single-crystal surfaces. Part 1. Behaviour at low-index faces, J. Electroanal. Chem. 407 (1996) 1–11.
[49] G. Feng, T. Niu, X. You, Z. Wan, Q. Kong, S. Bi, Studies on the effect of electrode pretreatment on the coverage of self-assembled monolayers of dodecanethiol on gold by electrochemical reductive desorption determination, Analyst. 136 (2011) 5058–5063.

[50] M.M. Walczak, C.A. Alves, B.D. Lamp, M.D. Porter, Electrochemical and X-ray photoelectron spectroscopic evidence for differences in the binding sites of alkanethiolate monolayers chemisorbed at gold, J. Electroanal. Chem. 396 (1995) 103–114.
[51] H. Li, P. Dauphin-Ducharme, G. Ortega, K.W. Plaxco, Calibration-Free Electrochemical Biosensors Supporting Accurate Molecular Measurements Directly in Undiluted Whole Blood, J. Am. Chem. Soc. 139 (2017) 11207–11213.
[52] A. Makaraviciute, X. Xu, L. Nyholm, Z. Zhang, Systematic Approach to the Development of Microfabricated Biosensors: Relationship between Gold Surface Pretreatment and Thiolated Molecule Binding, ACS Appl. Mater. Interfaces. 9 (2017) 26610–26621.
[53] R.P. Frankenthal, D.E. Thompson, The Anodic Behavior of Gold in Sulfuric Acid Solutions Effect of Chloride and Electrode Potential, J. Electrochem. Soc. 123 (1976) 799–804.
[54] A. Kolics, A. E. Thomas, A. Wieckowski, 36 Cl labelling and electrochemical study of chloride adsorption on a gold electrode from perchloric acid media, J. Chem. Soc. Faraday Trans. 92 (1996) 3727–3736.
[55] S. Ye, C. Ishibashi, K. Uosaki, Anisotropic Dissolution of an Au(111) Electrode in Perchloric Acid Solution Containing Chloride Anion Investigated by in Situ STMThe Important Role of Adsorbed Chloride Anion, Langmuir. 15 (1999) 807–812.
[56] D.A.J. Rand, R. Woods, A study of the dissolution of platinum, palladium, rhodium and gold electrodes in 1 m sulphuric acid by cyclic voltammetry, J. Electroanal. Chem. Interfacial Electrochem. 35 (1972) 209–218.
[57] J. Solla-Gullón, A. Aldaz, J. Clavilier, Ultra-low platinum coverage at gold electrodes and its effect on the hydrogen reaction in acidic solutions, Electrochimica Acta. 87 (2013) 669–675.
[58] Y. Sugawara, T. Okayasu, A.P. Yadav, A. Nishikata, T. Tsuru, Dissolution Mechanism of Platinum in Sulfuric Acid Solution, J. Electrochem. Soc. 159 (2012) 779–786.
[59] A.P. Yadav, A. Nishikata, T. Tsuru, Effect of halogen ions on platinum dissolution under potential cycling in 0.5M H2SO4 solution, Electrochimica Acta. 52 (2007) 7444–7452.
[60] H. Angerstein-Kozlowska, B.E. Conway, A. Hamelin, L. Stoicoviciu, Elementary steps of electrochemical oxidation of single-crystal planes of Au—I. Chemical basis of processes involving geometry of anions and the electrode surfaces, Electrochimica Acta. 31 (1986) 1051–1061.
[61] P. Zelenay, L.M. Rice-Jackson, A. Wieckowski, Radioactive labeling study of sulfate/bisulfate adsorption on smooth gold electrodes, J. Electroanal. Chem. Interfacial Electrochem. 283 (1990) 389–401.
[62] U. Zhumaev, A.V. Rudnev, J.-F. Li, A. Kuzume, T.-H. Vu, T. Wandlowski, Electro-oxidation of Au(111) in contact with aqueous electrolytes: New insight from in situ vibration spectroscopy, Electrochimica Acta. 112 (2013) 853–863.
[63] G.J. Edens, X. Gao, M.J. Weaver, The adsorption of sulfate on gold(111) in acidic aqueous media: adlayer structural inferences from infrared spectroscopy and scanning tunneling microscope, J. Electroanal. Chem. 375 (1994) 357–366.

[64] T. Kondo, J. Morita, K. Hanaoka, S. Takakusagi, K. Tamura, M. Takahasi, J. Mizuki, K. Uosaki, Structure of Au(111) and Au(100) Single-Crystal Electrode Surfaces at Various Potentials in Sulfuric Acid Solution Determined by In Situ Surface X-ray Scattering, J. Phys. Chem. C. 111 (2007) 13197–13204.
[65] F. Silva, A. Martins, Surface structural effects on specific adsorption of oxoanions on gold single crystal electrodes, J. Electroanal. Chem. 467 (1999) 335–341.
[66] G. Horányi, E.M. Rizmayer, P. Joó, Radiotracer study of the adsorption of Cl− and HSO4− ions on a porous gold electrode and on underpotential deposited metals on gold, J. Electroanal. Chem. Interfacial Electrochem. 152 (1983) 211–222.
[67] K. Juodkazis, J. Juodkazyt≒, V. Jasulaitien≒, A. Lukinskas, B. Šebeka, XPS studies on the gold oxide surface layer formation, Electrochem. Commun. 2 (2000) 503–507.
[68] K. Nygren, M. Folkenant, U. Jansson, L. Nyholm, Influence of Nanoeffects on the Oxidation of Cr–C/Ag Thin Films Containing Silver Nanoparticles, ChemElectroChem. 4 (2017) 418–429.
[69] R. Owczarzy, Y. You, B.G. Moreira, J.A. Manthey, L. Huang, M.A. Behlke, J.A. Walder, Effects of Sodium Ions on DNA Duplex Oligomers: Improved Predictions of Melting Temperatures, Biochemistry. 43 (2004) 3537–3554.
[70] W.A. Kibbe, OligoCalc: an online oligonucleotide properties calculator, Nucleic Acids Res. 35 (2007) W43–W46.
[71] P. Gong, R. Levicky, DNA surface hybridization regimes, Proc. Natl. Acad. Sci. 105 (2008) 5301–5306.
[72] A.W. Peterson, R.J. Heaton, R.M. Georgiadis, The effect of surface probe density on DNA hybridization, Nucleic Acids Res. 29 (2001) 5163–5168.
[73] E. Stern, R. Wagner, F.J. Sigworth, R. Breaker, T.M. Fahmy, M.A. Reed, Importance of the Debye Screening Length on Nanowire Field Effect Transistor Sensors, Nano Lett. 7 (2007) 3405–3409.
[74] D. E. Yates, S. Levine, T. W. Healy, Site-binding model of the electrical double layer at the oxide/water interface, J. Chem. Soc. Faraday Trans. 1 Phys. Chem. Condens. Phases. 70 (1974) 1807–1818.
[75] A. Yamada, S. Mohri, M. Nakamura, K. Naruse, A Simple Method for Decreasing the Liquid Junction Potential in a Flow-through-Type Differential pH Sensor Probe Consisting of pH-FETs by Exerting Spatiotemporal Control of the Liquid Junction, Sensors. 15 (2015) 7898–7912.
[76] G.S. Manning, Limiting Laws and Counterion Condensation in Polyelectrolyte Solutions I. Colligative Properties, J. Chem. Phys. 51 (1969) 924–933.
[77] R.B.M. Schasfoort, P. Bergveld, R.P.H. Kooyman, J. Greve, Possibilities and limitations of direct detection of protein charges by means of an immunological field-effect transistor, Anal. Chim. Acta. 238 (1990) 323–329.
[78] R.L. Stoop, M. Wipf, S. Müller, K. Bedner, I.A. Wright, C.J. Martin, E.C. Constable, W. Fu, A. Tarasov, M. Calame, C. Schönenberger, Competing surface reactions limiting the performance of ion-sensitive field-effect transistors, Sens. Actuators B Chem. 220 (2015) 500–507.
[79] S.U. Akki, C.J. Werth, Critical Review: DNA Aptasensors, Are They Ready for Monitoring Organic Pollutants in Natural and Treated Water Sources?, Environ. Sci. Technol. 52 (2018) 8989–9007.

[80] R. Liu, Z. Yang, Q. Guo, J. Zhao, J. Ma, Q. Kang, Y. Tang, Y. Xue, X. Lou, M. He, Signaling-Probe Displacement Electrochemical Aptamer-based Sensor (SD-EAB) for Detection of Nanomolar Kanamycin A, Electrochimica Acta. 182 (2015) 516–523.
[81] Y. Xiao, A.A. Lubin, B.R. Baker, K.W. Plaxco, A.J. Heeger, Single-step electronic detection of femtomolar DNA by target-induced strand displacement in an electrode-bound duplex, Proc. Natl. Acad. Sci. 103 (2006) 16677–16680.
[82] Z. Zhang, C. Tao, J. Yin, Y. Wang, Y. Li, Enhancing the response rate of strand displacement-based electrochemical aptamer sensors using bivalent binding aptamer-cDNA probes, Biosens. Bioelectron. 103 (2018) 39–44.
[83] D. Bizzotto, I.J. Burgess, T. Doneux, T. Sagara, H.-Z. Yu, Beyond Simple Cartoons: Challenges in Characterizing Electrochemical Biosensor Interfaces, ACS Sens. 3 (2018) 5–12.
[84] E. Delamarche, B. Michel, H. Kang, Ch. Gerber, Thermal Stability of Self-Assembled Monolayers, Langmuir. 10 (1994) 4103–4108.

Acta Universitatis Upsaliensis

Digital Comprehensive Summaries of Uppsala Dissertations from the Faculty of Science and Technology 1882

Editor: The Dean of the Faculty of Science and Technology

A doctoral dissertation from the Faculty of Science and Technology, Uppsala University, is usually a summary of a number of papers. A few copies of the complete dissertation are kept at major Swedish research libraries, while the summary alone is distributed internationally through the series Digital Comprehensive Summaries of Uppsala Dissertations from the Faculty of Science and Technology. (Prior to January, 2005, the series was published under the title "Comprehensive Summaries of Uppsala Dissertations from the Faculty of Science and Technology".)

Distribution: publications.uu.se
urn:nbn:se:uu:diva-397807

ACTA
UNIVERSITATIS
UPSALIENSIS
UPPSALA
2020